Doped SrSnO$_3$ for low strain BaTiO$_3$ ferroelectric field effect transistors

Eric Brand

August 10, 2021

Abstract

In this thesis, the use of doped SrSnO$_3$ for low strain BaTiO$_3$ ferroelectric field effect transistors (FeFETs) is considered. These low strain BaTiO$_3$ FeFETs possibly have memristive properties, which can be exploited for use in neuromorphic computing. Strain engineering of BaTiO$_3$ can lead to novel ferroelectric phases. Low strain BaTiO$_3$ can posses ferroelectric a/c domain, as has be shown by A. Everhardt(2017). The a/c domains have different polarisation time constants, the different polarisation time constants can be utilised for implementing the spike-time-dependent-plasticity (STDP) mechanism in an FeFET. To produce a/c domains the BaTiO$_3$ is strained by doped SrSnO$_3$. A doped SrSnO$_3$ film is grown on a SrTiO$_3$ substrate. The BaTiO$_3$ is grown under low strain on the doped SrSnO$_3$ film. The master research project focusses on using Nb doped SrSnO$_3$ as an n-channel material in a FeFET and the electrical characterisation of the Ti/BaTiO$_3$/Y$_{0.05}$Sr$_{0.95}$SnO$_3$ stack for the use of Ti as an gate electrode.

Contents

1 Introduction

The master research project is focused on the implementation of doped $SrSnO_3$ in low strain $BaTiO_3$ ferroelectric field effect transistors (FeFETS). These low strain $BaTiO_3$ FeFETs may have memristive properties and be suitable for neuromorphic computing. The interest in neuromorphic computing can be understood in the context of the CogniGron programme. CogniGron, or the *Groningen Cognitive Systems and Materials Center*, is an interdisciplinary collaboration within the Faculty of Science of the University of Groningen. The *Zernike Institute for Advanced Materials* and the *Bernoulli Institute for Mathematics, Computer Science and Artificial Intelligence* collaborate together to advance the field of cognitive computing. The term cognitive computing can also be understood as neuromorphic computing or brain-inspired computing. The goal of the collaboration is to implement new materials with memrisitive properties in cross-linked networks at the nano-scale. The new material structures should lead to more efficient and denser circuit than present neuromorphic computerchips such as TrueNorthTM from IBM[1]. The institutes will contribute to this goal from their various disciplines, namely Material Science, Artificial Intelligence, Computer Science and Mathematics, see Fig. 1.
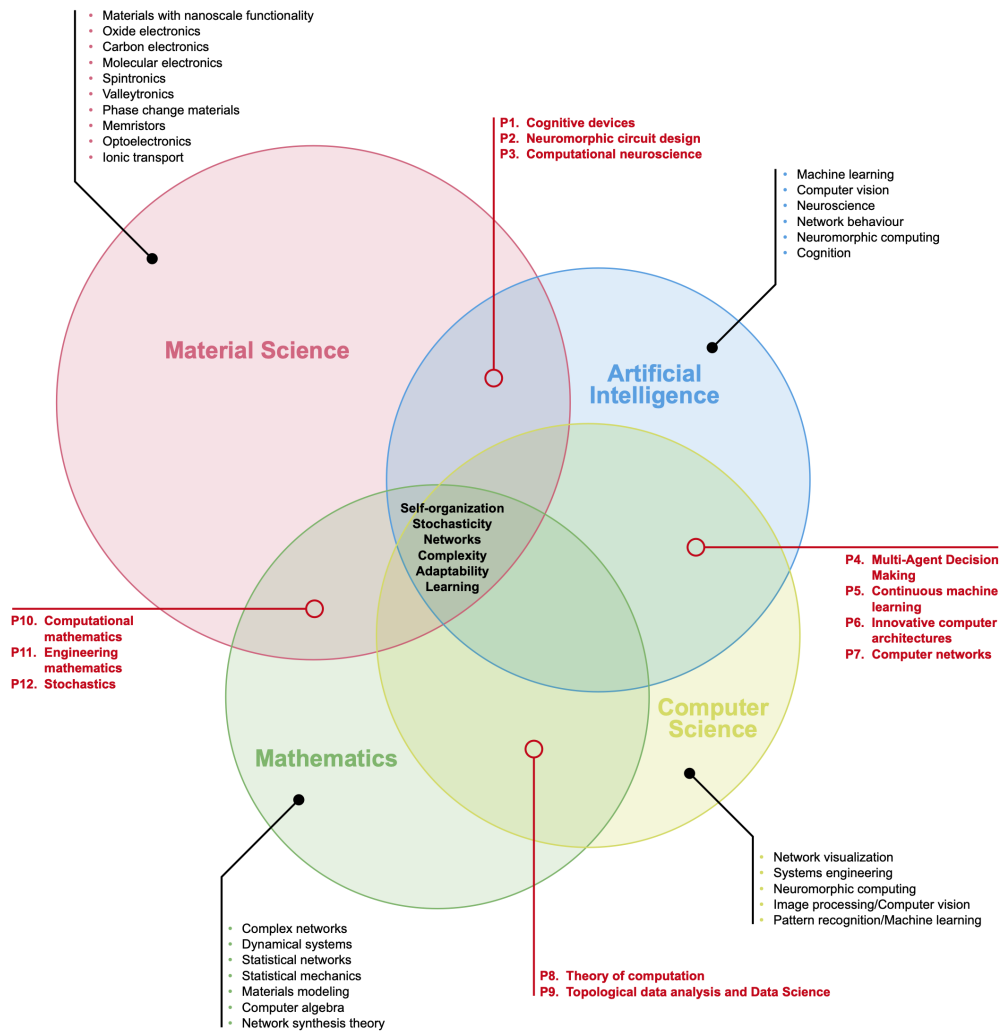

Figure 1: Overview of expertises involved in CogniGron and their overlap in regards to neuromorphic engineering. [2]

The neuromorphic engineering of low strain BaTiO$_3$ FeFETs consists of straining the BaTiO$_3$ films by using doped SrSnO$_3$ films. The BaTiO$_3$ and SrSnO$_3$ films are grown on a SrTiO$_3$ substrate. The doped SrSnO$_3$ functions as an intermediate layer to apply a low strain to the BaTiO$_3$, using SrTiO$_3$ will not work due to the lattice mismatch with the BaTiO$_3$ being too large for epitaxial growth. The low strain in the BaTiO$_3$ film can lead to the formation of novel ferroelectric phases. These novel ferroelectric phases lead to the BaTiO$_3$ film having an multi-domain structure with out-of-plane and in-plane polarisations. The different polarisations posses different polarisation time constants, which affects their response to input signals. The implementation of an multi-domain ferroelectric BaTiO$_3$ in a FeFET could lead to an device with memristive properties. The memristive properties can be exploited for use in neuromorphic computing. However the novel ferroelectric phases were not found during the master research project.

The fabrication of BaTiO$_3$ FeFETs strained by doped SrSnO$_3$ requires the optimisation of the different components of the FeFET. The components of an FeFET involve an ferroelectric layer, an conduction layer and the electrodes. The optimisation of the ferroelectric layer requires the strain engineering of BaTiO$_3$ with doped SrSnO$_3$. The conduction layer should consist of n-doped SrSnO$_3$. The electrodes optimisation requires the consideration of a wide range of metals to fabricat a properly functioning FeFET. The thesis will focus on optimising the conduction layer by considering the use of Nb as a n-dopant in SrSnO$_3$. Furthermore the conduction mechanisms over a BaTiO$_3$/SrSnO$_3$ stack with Ti electrodes are analyzed to study the viability of Ti as a gate electrode in an FeFET.

The thesis consists of three theory sections followed by the methodology. The theory sections explain the general principles of neuromorphic engineering followed by the more specific discussion of novel ferroelectric phases in strained BaTiO$_3$. The last theory section discusses the low strain BaTiO$_3$ FeFET. The experimental part of the thesis is described in the last two chapters. One chapter focusses on the use of Nb doped SrSnO$_3$ for the use as n-channel layer in a low strain BaTiO$_3$ FeFET, this chapter mostly focusses on surface and structural characterisation. The other chapter focusses on the electrical characterisation of the Ti/BaTiO$_3$/Y$_{0.05}$Sr$_{0.95}$SnO$_3$ stack to discuss the use of Ti as a gate electrode in a low strain BaTiO$_3$ FeFEt.

2 Neuromorphic Engineering

Neuromorphic engineering concerns itself with the implementation of neuromorphic computing in physical systems. Neuromorphic computing concerns itself with the imitation of the data processing in the human brain. The field of neuromorphic computing is formed at the intersection of mathematics, computer science and artificial intelligence. A popular mechanism describing the data processing in the brain is the "spike time dependent plasticity" (STDP) mechanism. The implementation of the STDP mechanism in an physical, electrical system is possible utilizing memristive systems. These memristive systems are based on the working principles of the memristor, the fourth fundamental two terminal circuit element. This section introduces the neuromorphic field and explains the working principles of the STDP mechanism and memristive systems.

The most spectacular and impactful claim that the neuromorphic field makes is the potential to bypass the "Moore's crisis"[3]. This crisis refers to the breaking down of Moore's law, which states that the number of transistors in an integrated circuit double every two years. The reason for the breaking down of Moore's law is due to the silicon based transistors reaching their physical limit. The "Moore's crisis" can possibly be bypassed by changing the computer architecture with the goal of increasing computing power even when the silicon based transistors have reached their physical limit. The current computer architectures are based on the Von-Neumann architecture, resulting in store-program machines. In a store-program machine the data and program instructions are stored in a Memory Unit (MU) connected to a Central Processing Unit (CPU). The data and instructions are bussed from the MU to the CPU, which executes the arithmetic and logic operations. The data bussing in the Von-Neumann architecture is the bottleneck for how fast data can be processed, the so called Von-Neumann bottleneck. A neuromorphic computer architecture may incorporate the data storing and processing in the same unit such that the limits imposed by the Von-Neumann bottleneck are irrelevant[4]. So the switching from a Von-Neumann architecture to an neuromorphic architecture could increase the computing power even when the physical limit of the transistor size is reached and functionally extend Moore's law further into the future.
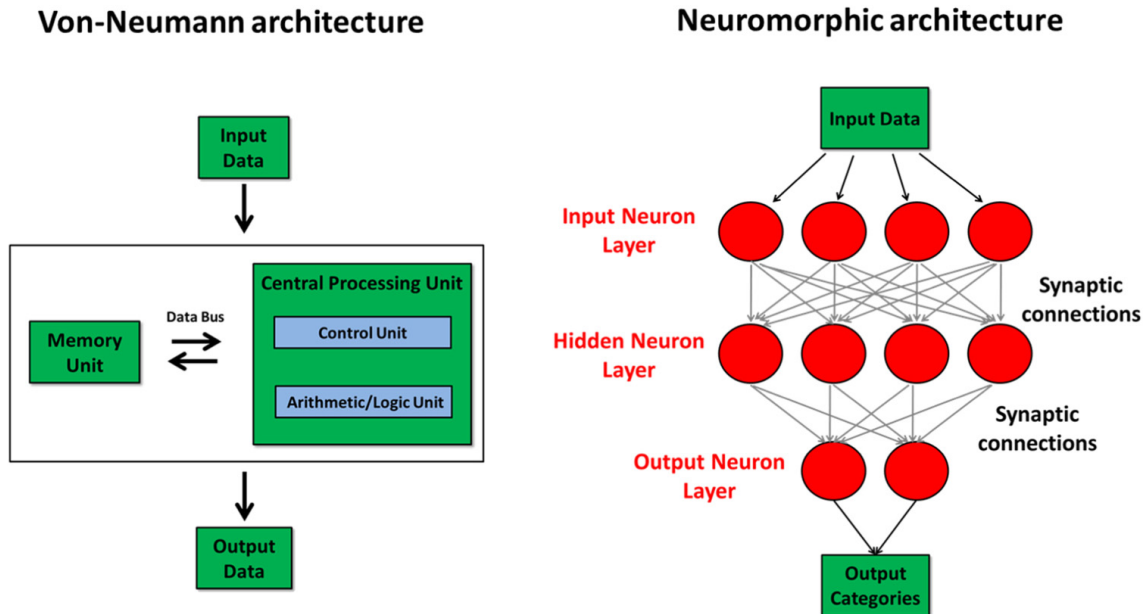

Figure 2: Differences in data processing between the von-Neumann and neuromorphic architecture[4].

The complete replacement of the Von-Neumann architecture by the neuromorphic architecture is in practice unlikely. The main interest in neuromorphic computing is based on the difference

in data processing compared to the Von-Neumann architecture. Compared to the Von-Neumann architecture, neuromorphic architectures have a high logical reliability, but low arithmetic precision. This difference in data processing is due to the focus of the neuromorphic architecture on imitating the pattern seeking human brain, necessitating high logical reliability and a lesser importance of arithmetic precision. The definition of neuromorphic computing indicating a nervous system like implementation of computing. The imitation of the human brain in neuromorphic computing is based around mathematical simplifications of the data processing in the nervous system. This reductionist view on the human brain has been discussed by von Neumann himself in his incomplete Silliman lectures[5]. A popular framework for data processing in the human brain is the "spike time dependent plasticity mechanism" (STDP) mechanism. This mechanism will be discussed in the following section and clarify how a biological system can be reduced to a set of mathematical functions and be implemented into an physical (electrical) system.

2.1 Spike time dependent plasticity

The human brain is a complex part of the nervous system and responsible for data processing. To imitate the brain in neuromorphic computing, this biological system has to be reduced to an algorithm. An algorithm for signal processing in the nervous system is provided by the "spike time dependent plasticity mechanism" (STDP) mechanism[6]. The STDP mechanism is a learning algorithm using spike-based computations, specifically utilizing the relative timing between spikes. This method of spike-based computing is inspired by the interaction between synapses in the human brain.
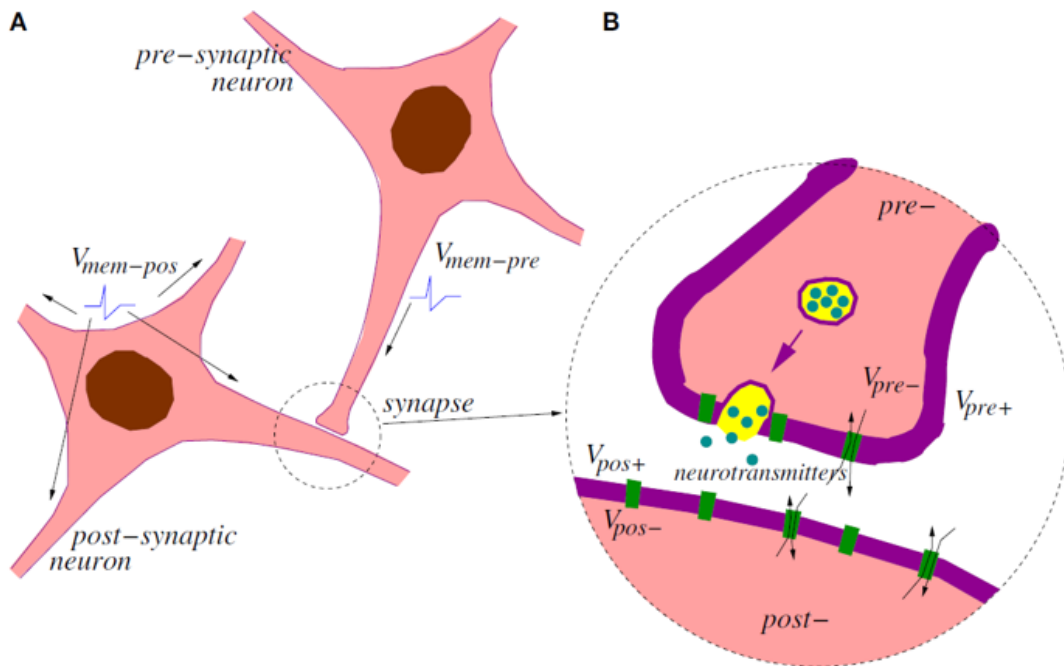
Figure 3: Schematic overview of the synapse between the pre and post-synaptic neuron. Notice the yellow vesicle releasing neurotransmitters under the influence of the pre-synaptic pike.[6]

The interaction between synapses in the brain can be described as visualised in Fig. 3. A pre-synaptic neuron sends a pre-synaptic voltage spike, $V_{mem-pre}(t)$, to the synaptic junction. The voltage spikes are the consequence of the flow of membrane voltages, membrane voltages are generated by the difference in voltage between the inside and outside of the cellular membrane, so $V_{mem-pre}(t)=V_{pre+}$ - V_{pre-} and $V_{mem-pos}(t)=V_{pos+}$ - V_{pos-}. When the pre-synaptic voltage spike reaches the synapse, synaptic vesicles will fuse with the membrane releasing neurotransmitters into

the inter cellular space between the post and pre-synaptic neuron. The neurotransmitters change the conductivity of the membrane of the post-synaptic neuron, if the conductivity changes enough a new post-synaptic voltage spike will be generated. The conductivity change is integrated over multiple pre-synaptic spikes possibly coming from different synapses each with their own synaptic strength.

The synaptic strength can be considered as a weight, w, which determines the efficacy of the contribution of a pre-synaptic spike to an action performed by the post-synaptic neuron. The weight can be changed by the interaction of the pre-synaptic and post-synaptic spike at the synapse. The weight changing interaction between pre-synaptic and post-synaptic spikes is crucial for the functioning of the STDP learning algorithm. Specifically for STDP the weight change, Δw, is the consequence of the relative timing between the synaptic spikes, as can be seen in Fig. 4. So the change in weight can be expressed as:

$$\Delta w = \xi(\Delta T) \tag{1}$$

with $\Delta T = t_{pos}$ - t_{pre}. For positive ΔT, implying a relevant role of the pre-synaptic pike in generating the post-synaptic pike, the weight $\Delta w > 0$. Negative ΔT implies a irrelevant role of the pre-synaptic pike in generating a post-synaptic pike, so $\Delta w < 0$. Furthermore a smaller $|\Delta T|$ implies a larger value of Δw. Mathematically the STDP learning function can then be defined as:

$$\xi(\Delta T) = \begin{cases} a^+ e^{-\Delta T/\tau^+} & \text{if } \Delta T > 0 \\ -a^- e^{-\Delta T/\tau^-} & \text{if } \Delta T < 0 \end{cases}$$

More complexity can be introduced to the basic STDP learning function by considering inhibitory synapses, implying negative weight, w. More exotic STDP learning functions are also possible and understanding these exotic function may be of importance to establish a connection between the STDP mechanism and the memristive properties of certain materials. The following section will introduce memristivity and show the implementation of a STDP like mechanism in a physical system.
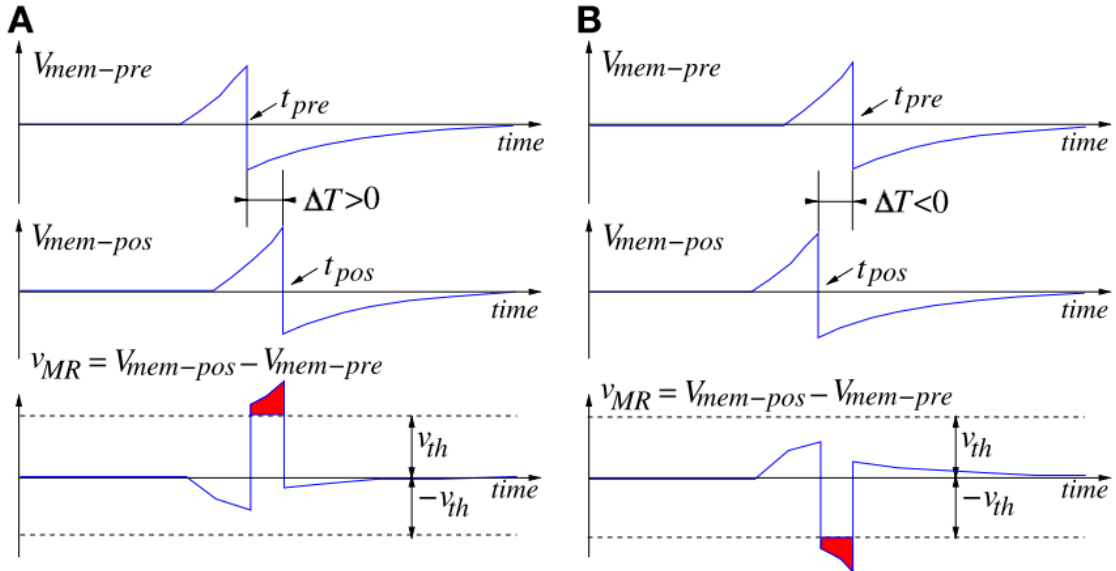

Figure 4: Overview of pre and post-synaptic spike interactions for $\Delta T > 0$ (A) and $\Delta T < 0$ (B). The voltage V_{MR} stands for the change in membrane voltage.[6]

2.2 Memristors and memristive systems

Memristive systems are a popular topic of research, because the properties of these systems can be utilized for neuromorphic engineering. At the basis of the memristive system stands the memristor. The memristor is a two terminal element used in electrical circuit building. In circuit building the conventional three fundamental two terminal elements are the resistor, the capacitor and the inductor. The behaviour of these elements is described by a linear relationship between two of the four fundamental circuit variables, namely the voltage v, current i, electric charge q and magnetic flux ρ. However in 1971 Chua [7] proposed a fourth basic circuit element, the memristor. This two terminal circuit element links the magnetic flux to the electric charge through the memristance M, see Fig. 5.
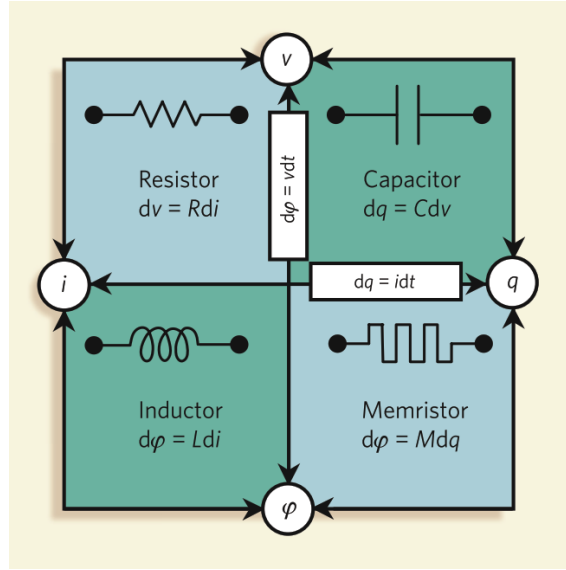

Figure 5: The complete quartet of fundamental two terminal circuit elements. Six relations may be formed based on pairs of the four fundamental circuit variables. Two based on time integrals of current and voltage and four basic circuit elements[8].

The two terminal passive memristor element has an unique non-linear feature not observed in the other three fundamental circuit elements[9]. When describing the current-voltage characteristics of the now four fundamental circuit elements, the classical three all show a linear relationship between current and voltage under the application of a sinusoidal input voltage. In case of the resistor, R, the linear relationship in the IV-plane can be readily seen. The linear relationship between current and voltage is shifted by ±90 phase difference for the capacitor and inductor. The memristor instead shows a pinched hysteresis loop with a zero crossing in the IV-plane, this hysteretic behaviour evidences the non-linear behaviour of the memristor, see Fig. 6.
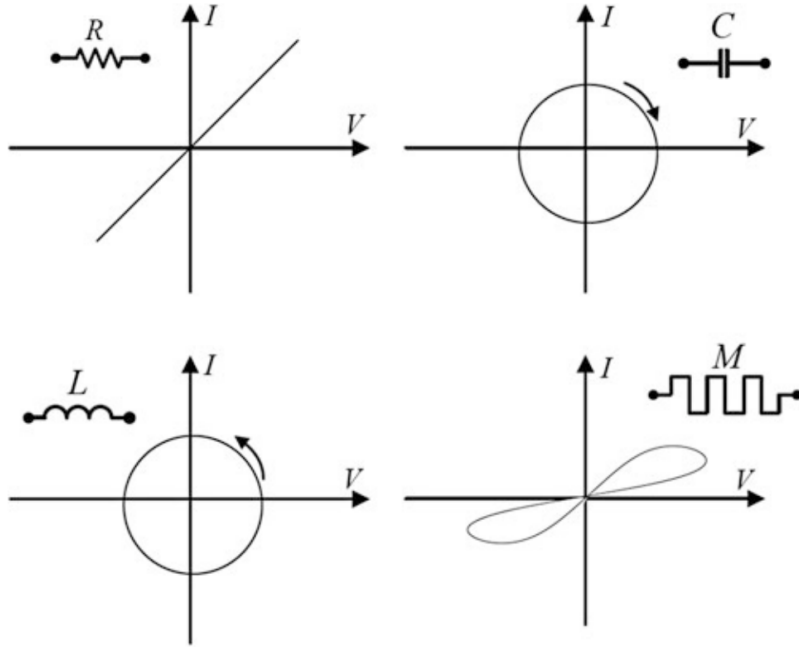
Figure 6: Current-voltage characteristics of the four fundamental two terminal elements. Shown the resistor(R), capacitor(C), inductor(L) and memristor(M)[9].

Considering the non-linear behaviour of the memristor under the application of a time-varying voltage, it is possible to define two types of memristors. First there is the charge-dependent or current-controlled memristor:

$$v(t) = M(q(t))i(t) \tag{2}$$

$$M(q) = \frac{d\theta(q)}{dq} \tag{3}$$

and secondly the flux-dependent or voltage-controlled memristor:

$$i(t) = W(\phi(t))v(t) \tag{4}$$

$$W(\phi) = \frac{dq(\phi)}{d\phi} \tag{5}$$

with $M(q)$ and $W(\phi)$ respectively being the memristance and memductance with the units of resistance and conductance. The given relations show the nonlinear aspects of the memristor.

The nonlinear characteristics of the memristor lead to the consideration that the memristor is only a special case of a more general class of dynamic systems, called the memristive systems [10]. Generalizing the equations describing the nonlinear characteristics of the memristor gives the following set of equations for the current-controlled or charge-dependent memristive system:

$$v(t) = R(x, i(t), t)i(t) \tag{6}$$

$$\frac{dx}{dt} = f(x, i(t), t) \tag{7}$$

with R being the time-dependent resistance which also depends on the state, x, of the system. The rate of change of the system state, x, depends on the systems history. The generalised equations can be used to model or describe physical memristive systems. In 2008 a memristor was made by

Hewlett Packard based on dopant drift[11]. A few years later in 2012, an ferroelectric memristor was made by the Grollier group[12]. The ferroelectric memristor from the Grollier group is based on an ferroelectric tunnel junction (FTJ) instead of an ferroelectric field effect transistor, however the ferroelectric aspects of the memristor may still show similarities.

The ferroelectric memristor shows memristive behaviour as can be seen in Fig. 7. The memristive behaviour is the consequence of the voltage-controlled domain configurations in the ferroelectric tunnel junction. The resistance of the ferroelectric tunnel junction depends on the ratio between the down an up domains, so a possible state variable s can be defined based on the relative fraction of down domains:

$$s = (\frac{1}{R} - \frac{1}{R_{ON}})/(\frac{1}{R_{OFF}} - \frac{1}{R_{ON}}) \tag{8}$$

with R being the measured resistance of the ferroelectric tunnel junction. The variables RON and R_{OFF} respectively stand for a low resistance fully up polarised state and a high resistance fully down polarised state. The relative fraction of down domains depends on the amplitude, amount and duration of the applied voltage pulses and on the fraction of already down polarised domains. So the rate of change of the state variable s depends on the state itself and the history of applied voltage pulses. Thus it is possible to assign a memristance to the ferroelectric tunnel junction. The result is an well defined FTJ memristor.
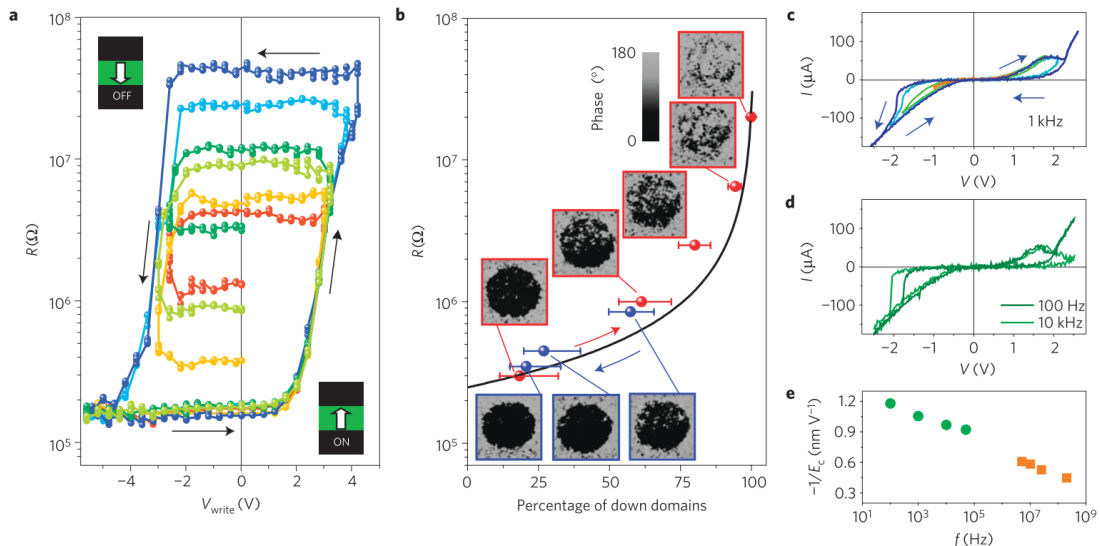

Figure 7: Memristive characteristics of ferroelectric tunnel junction.(a) Resistance switching under consecutive voltage pulses.(b) Resistance dependence on percentage of down domains.(c),(d) Pinched IV hysteresis loop for different frequencies.(e) Switching electric field dependent on frequency[12].

The master research project falls under the scope of research into an memristive ferroelectric field effect transistor (FeFET). The FeFET and FTJ devices differ considerably, FTJs are two terminal devices with the current flow through the ferroelectric component, while FeFETs are three terminal devices in which the ferroelectric component modulates the current flow through another channel. However in both cases the resistance should show a dependendcy on the ratio between up and down polarized domains. Furhtermore the polarization switching should occur on the same time scale in an FTJ as in a FeFET, so comparing the behaviours of the pinched IV hysteresis loops over a range of frequencies is usefull.

3   Novel ferroelectric phases in BaTiO3

The scope of the project involves working towards the fabrication of an memristive ferroelectric field effect transistor (FeFET). The ferroelectric component in the FeFET is an $BaTiO_3$ film. The use of $BaTiO_3$ (BTO) as an ferroelectric has an long history in industry dating back to the second world war. The ferroelectric properties of BTO are caused by its perovskite crystal structure. Perovksite BTO has been extensively studied as a bulk crystal, however in thin film applications the research is far from finished. The study of the strained films BTO is interesting because of the novel ferroelectric phases present. The novel ferroelectric phases in BTO have been experimentally verified by the author A. Everhardt[13]. The following sections will define ferroelectricity and the rich ferroelectric phase behaviour under strain. Furthermore strain in ferroelectric films also leads to flexoelectricity and polarisation rotation, these phenomena will also be discussed.
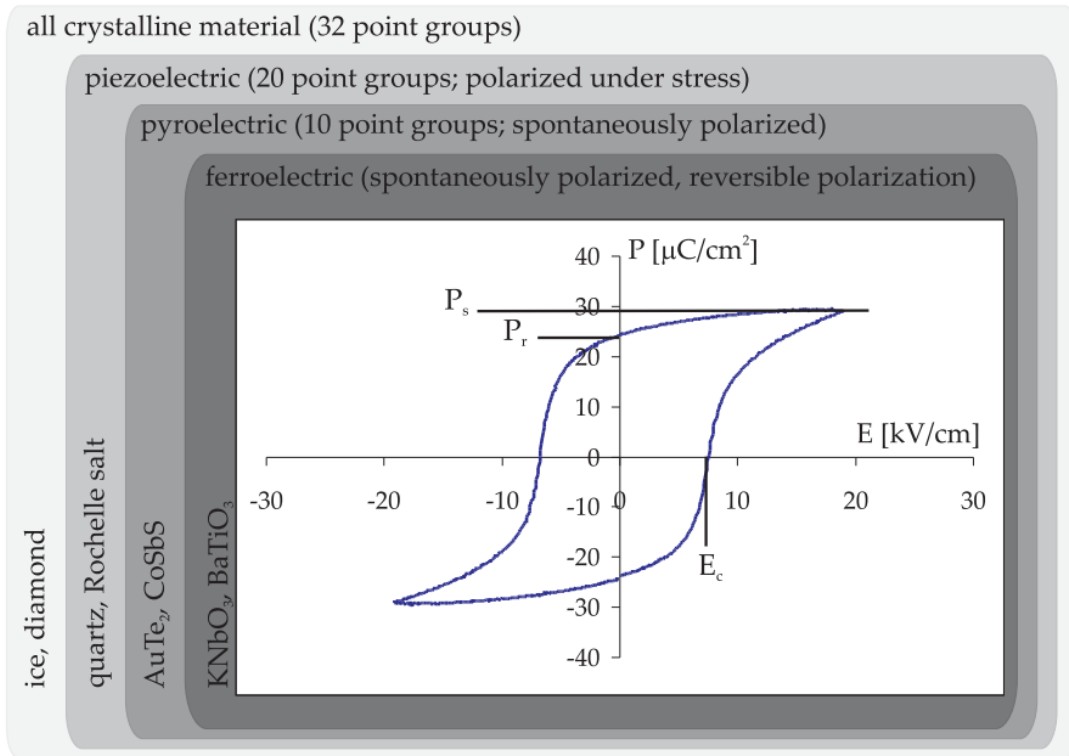

Figure 8: Ferroelectric materials as subset of point groups. Out of all the possible point groups a crystalline material can belong to, only 10 point represent possible ferroelectric materials. [14]

3.1   Ferroelectricity

Ferroelectricity can only occur for materials which posses a crystal structure belonging to a specific set of point groups[?][14]. A point group is a set of symmetry operations which leaves the crystal structure unchanged. The symmetry operations being translation, reflection, rotation and inversion. All crystalline materials can be described by a set of 32 point groups. A subset of 20 point groups do not have inversion symmetry, this describes non-centrosymmetric materials and indicates possible piezoelectricity. Piezoelectric materials display a change in electric polarization under mechanical stress and vice versa. Further reduction of symmetry produces another set of 10 point groups, these 10 point groups posses a polar axis and form the group of pyroelectric materials, the polar axis implies that every symmetry operation leaves at least two points unmoved. Pyroelectrics with a reversible or switchable polarization are ferroelectric.
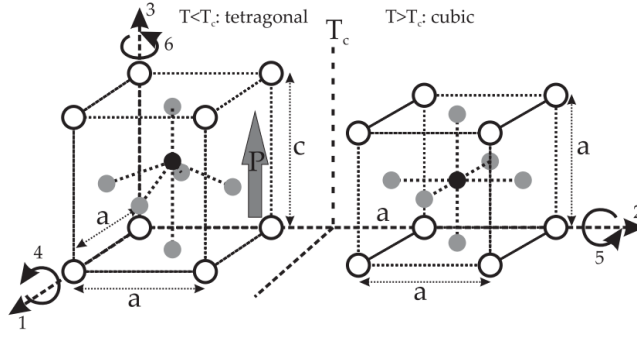
Figure 9: Perovskite (ABO_3) phase transition. The perovskite crystal undergoes a phase transition from cubic to tetragonal at the temperature T_C. The non-centrosymmetric tetragonal phase is ferroelectric. White and black spheres represent respectively the A and B cations, grey spheres represent the oxygen anions.[14]

The most technologically relevant ferroelectrics posses an perovskite (ABO_3) crystal structure. Examples of ferroelectric perovksites being $PbTiO_3$(PTO) and $BaTiO_3$(BTO). Despite PTO and BTO having the same crystal structure, their chemical difference leads to quite different ferroelectric behaviour. So the discussion of ferroelectricity in materials will focus on the specific case of BTO. In bulk, BTO has an paraelectric cubic phase (Pm3m) at high temperature. Lowering the temperature gives three ferroelectric phase transitions; cubic to tetragonal (393K), tetragonal to orthorhombic (278K) and orthorhombic to rhombohedral (183K)[15]. Ferroelectric phase transitions in $BaTiO_3$ are the consequence of the breaking of centrosymmetry and the deformation of the perovskite by shifting of the Ti^{4+} B-site cation[16], see Fig. 10.
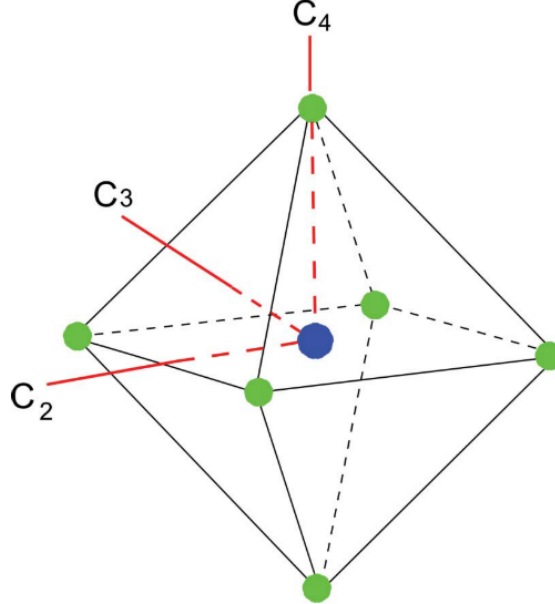

Figure 10: Potential shifts of the B-site cation (blue) in the oxygen (green) octahedral. In case of $BaTiO_3$, the Ti^{4+} shifts along the C_4, C_2 and C_3 axis.[17][16]

3.2 Ferroelectric phases

The polarization in ferroelectric materials does not have the same orientation in the whole thin film. The polarization orientations are organised in domains. Domains are crystal regions where order parameters such as polarization and strainn has the same orientation. The formation of domains occurs to lower the total energy of the system. The competing processes for lowering the energy of the system are domain formation and domain wall formation, which respectively decrease and increase the energy. In the case of thin films the depolarisation field is a significant driving force in domain formation[18]. Kittels law states that decreasing film thickness results in increasing depolarisation field. This is due to the scaling of the energy cost; domain formation scales with volume, while domain wall energy scales with area[19].
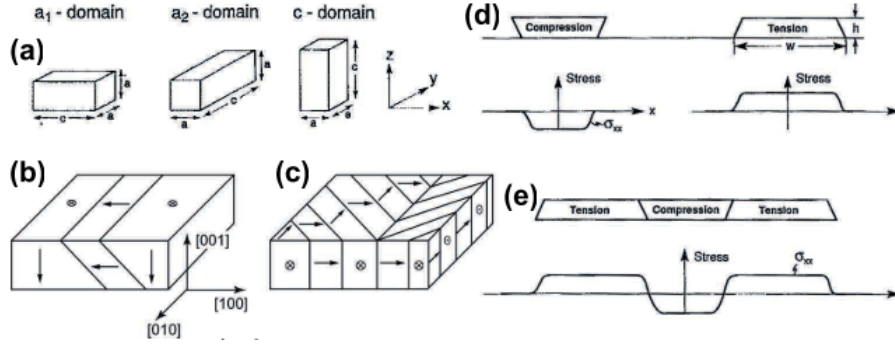

Figure 11: Ferroelastic domain formation. Substrate strain may lead to the development of domains with different lattice constants and polarization to minimize the strain energy[13].

The formation of domains in thin films is complex. Thin films are often strained by the substrate leading to relaxation mechanisms for stress release, see Fig. 11. In the case of an tetragonal film with $c>a$, three cases of strain relaxation can be considered. If the substrate parameter $a_S < c,a$, than c-domains are formed. If $a_S > c,a$, than the c-parameter of the film is in-plane and a_1,a_2 domains may be formed. In the case of $a < a_S < c$, it is possible that a/c domains will form.

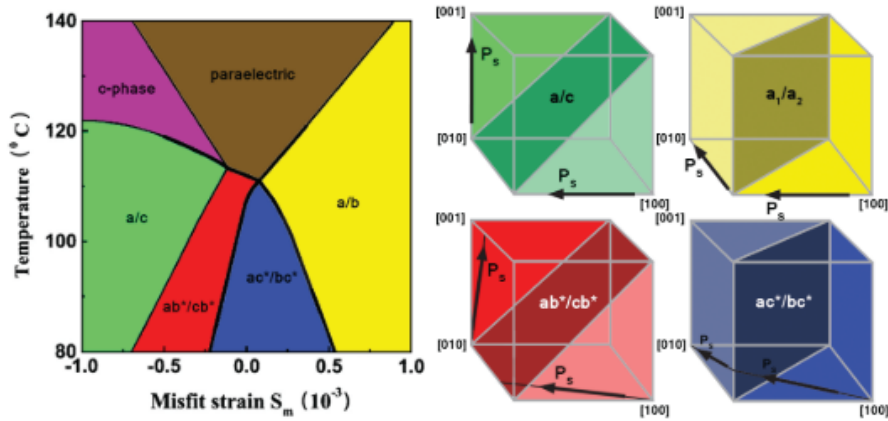Figure 12: Relation between misfit strain and domain ordering. Depending on temperature and strain between film and substrate, different domains form. The left side depicts the polarization orientation in the different domains.[20]

Considering the case $a < a_S < c$, in coherent epitaxial thin films it is possible to determine the minimum domain size by noting that a specific ratio of a and c domains leads to full strain

13

relaxation:

$$a \cdot N_c + c \cdot N_a = a_s \cdot N \tag{9}$$

where N_c, N_a and N are the number of unit cells in respectively c-domian, a-domains and in total. Under coherent strain, twinning will terminate the domains:

$$w_a = \frac{c}{sin(\alpha)} \tag{10}$$

where w_a is the width of the a-domain and α is the twin angle [13]. The factor c ensures that the a-domain gains exactly one c-lattice parameter in height to maintain coherency.
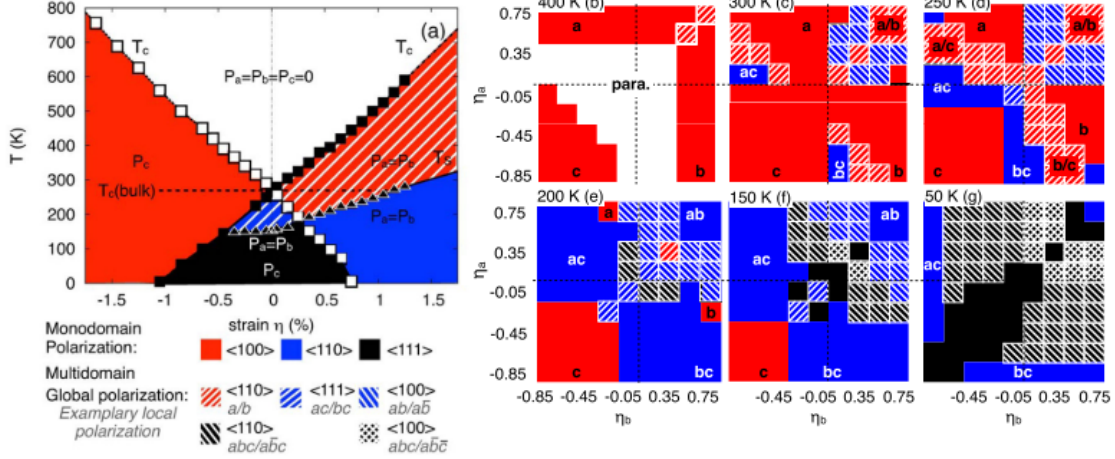

Figure 13: Multi-domain structure $BaTiO_3$. Leftside shows a isotropic temperature-strain diagram. Right side shows biaxial strain phase diagrams for different temperatures. [21]

Over the years extensive computationally studies have been performed to create phase diagrams of BaTiO$_3$ under strain. These computationally studies have become more sophisticated over the years starting with monoaxial strain[20] and expanding to biaxial strain[21], see Fig. 12 and 13. From Fig. 13 it can be observed that if BaTiO$_3$ is in its orthorhombic phase, biaxially strained domains can form. These biaxially strained domains have the potential to show multidomain structures under temperatures and strain for which monoaxially show a monodomain polarization. To conclude, the theory behind domain formation indicates complex ferroelectric phase behaviour for strained thin BaTiO$_3$ films.

3.3 Flexoelectricity

The effects of strain in thin BaTiO$_3$ films are not limited to only inducing novel ferroelectric phases in the films. The gradient of the strain through the film also leads to an spontaneous electrical polarisation, this effect is called flexoelectricity. The first studies on the practical application of flexoelectricity centered around the mechanical bending of ferroelectric crystals on a macroscopic scale[22][23]. The strain gradient in thin films is the consequence of a mismatch in lattice parameter between the substrate and the film. The mismatch in lattice parameter leads to relaxation of the film lattice parameter from highly strained at the substrate-film interface to unstrained far from the interface. The result being a strain gradient perpendicular to the substrate. A formal definition of the flexoelectric contribution to an intrinsic polarisation, P_i, is:

$$P_i = \chi_{ij}E_j + e_{ijk}u_{jk} + \mu_{klij}\frac{\delta u_{kl}}{\delta x_j} \tag{11}$$

14

where E_j, u_{jk} and $\frac{\delta u_{kl}}{\delta x_j}$ are respectively the applied electric field, the strain tensor and the spatial strain gradient. The terms χ_{ij}, e_{ijk} and μ_{klij} represent respectively the dielectric tensor, the piezo-electric tensor and the flexoelectric tensor. The flexoelectric tensor μ_{klij} is allowed in materials of any symmetry, while the piezoelectric tensor e_{ijk} is restricted to non-centrosymmetric crystals[24]. Thus flexoelectricity can occur in both ferroelectric and non-ferroelectric materials.

The flexoelectric polarisation causes interesting behaviour in ferroelectric thin films, such as pol-ing, polarisation switching and polarisation rotation. The poling and polarisation switching is the consequence of the flexoelectric field inducing a preferred polarisation orientation in the film. This can also be seen as the strain shifting the energy in the double well potential associated with ferro-electric polarisations, see Fig. 14. The assymetry in the double well potential leads to polarisation switching and poling.
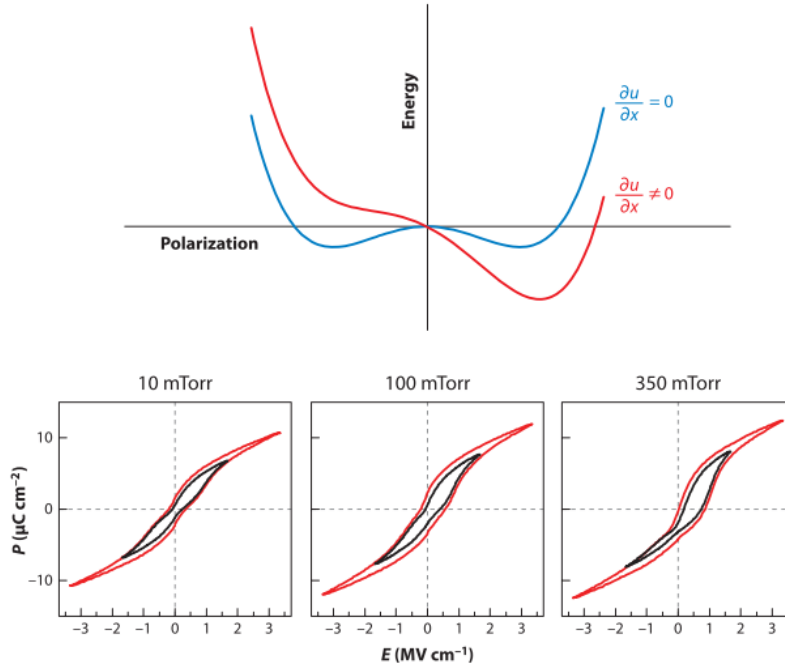

Figure 14: Strain induced shift in thermodyanamic potential. A strain gradient can skew the ferroelectric double-well potential in favour of a certain polarization state. Varying the oxygen pressure during the growth of a perovskite thin film influences the strain and thus shifts the ferroelectric hysteresis loop. [25][26]

The polarisation rotation in a thin film is caused by the interplay between the ferroelectric polarisation and the flexoelectric polarisation, this occurs when the direction of the strain and strain gradient differ. In a study of Catalan et al., a $PbTiO_3$ film was grown on a $SrRuO_3$ substrate and polarisation rotation occurred because of the presence of twin domains. The slanted domain walls of the twin domains led to an strain gradient parallel to the substrate and film. In the case of twinning between a/c domains, the out of plane polarisation will be rotated while the in plane polarisation will not rotate, see Fig. 15. Furthermore flexoelectricity can also cause voltage offsets in the ferroelectric hysteresis loop and smear the dielectric anomaly at the ferroelectric phase transition[24].
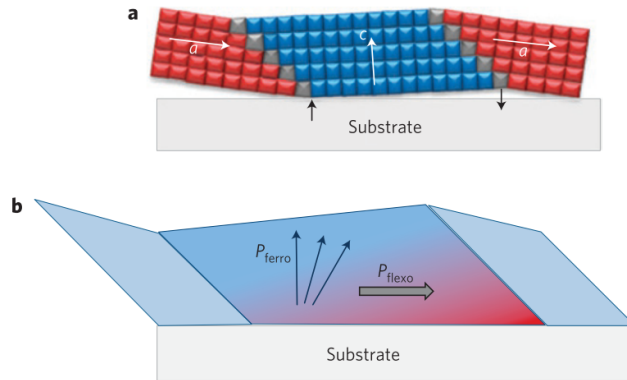
Figure 15: Polarisation rotation strained film. (a) Representation a/c domain structure thin film with twinning (b) The in-plane flexoelectric polarisation (grey) induces a rotation in the out-plane ferroelectric rotation (blue) [27].

The techniques used for the characterisation of flexoelectricity vary considerably in scope and practicality. The tools used for studying flexoelectricity by macroscopic bending are not suitable for studying flexoelectricity in strained thin films on the microscopic scale[22][23]. To study flexoelectricity at the microscopic scale electron microscopy[27], piezo force microscopy[28] and synchrotron techniques are used. The electron microscopy and synchrotron techniques provide in depth details of the strain and strain gradient, however these techniques are respectively invasive and resource consuming. Piezo force microscopy studies are non-invasive, but only useful to study films with thicknesses less than 5nm. Furthermore it is not possible to study strained films within a multi-layered structure using piezo force microscopy. Spectroscopy techniques, such as Raman spectroscopy, could be a useful tool for the non-invasive study of flexoelectricity in thin films[29]. Raman spectroscopy enables the study of materials possessing a non-centrosymmetric crystal structure. Ferroelectric materials posses a non-centrosymmetric crystal structure. Furthermore in the case of strained $BaTiO_3$, the orthorhombic crystal structure may reduce to lower symmetry crystal structures such as triclinic and monoclinic. These crystal crystal structures will also be Raman active. To summarise, electron microscopy and synchrotron techniques are the norm for studying flexoelectricity in thin films. Piezo force microscopy may be useful under specific circumstances. Spectroscopy techniques have the potential to contribute greatly to the understanding of flexoelectricity in thin films.

4 Ferroelectric field effect transistor

The goal of the project associated with my master thesis is to engineer a ferroelectric field effect transistor (FeFET) which implements a/c domains in strained $BaTiO_3$ and studies the memristive properties of such system, seef Fig. 17. These memristive properties can be used for brain inspired computing. The use of FeFETs for brain inspired computing is the topic of active research and implemented in neural networks[30][31]. The implementation of the spike-time dependent plasticity mechanism has been achieved by using HfO_2 based FeFETs[32]. This implementation is based on domains switching polarization and thereby altering the conductivity of the n-channel. Engineering the a/c domains in strained $BaTiO_3$ is a far from trivial exercise. Successful growth of a/c domains in a $BaTiO_3$ film has been achieved by A. Everhardt [13]. These $BaTiO_3$ films were grown on a $SrRuO_3$ substrate. However an $SrTiO_3$ substrate would be more practical for developing an FeFET with possible use in a commercial setting. The formation of a/c domains requires the lattice parameter of the substrate to be in between the a and c lattice parameter. The a and c lattice parameter of $BaTiO_3$ are respectively 3.99 Åand 4.03 Å, while the lattice parameter of the $SrTiO_3$ substrate is 3.91 Å. To still be able to epitaxially grow $BaTiO_3$ on a $SrTiO_3$ substrate, a spacer layer is necessary. The spacer layer used is $SrSnO_3$, however $SrSnO_3$ has a lattice parameter of 4.04 Åwhich is still larger than both the a and c lattice parameter of $BaTiO_3$. The lattice parameter of $SrSnO_3$ can be reduced by doping. A variety of dopants has been used for different concentrations, these dopants in include Y an Ti. Currently no a/c domains have been found in $BaTiO_3$ grown on doped $SrSnO_3$ with a $SrTiO_3$ substrate.

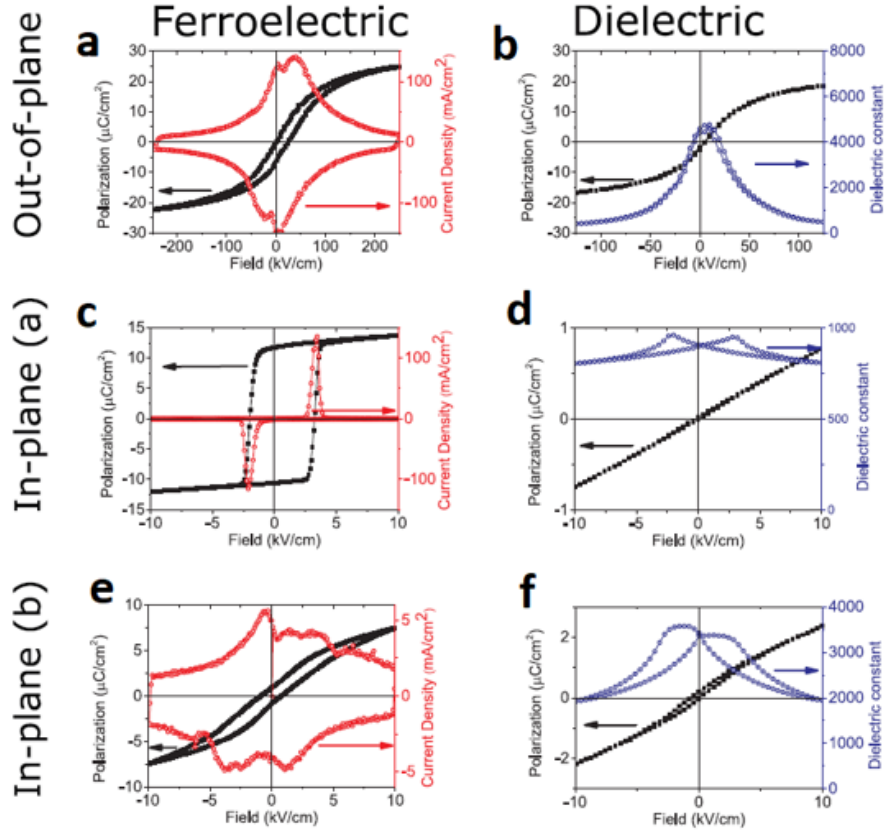Figure 16: Polarisation and dielectric behaviour for a/c domains measured along different axes. (a),(b) The out-of-plane direction or c-axis shows no ferroelectric behaviour and posses a high dielectric constant. (c),(d) The in-plane direction along the a-axis shows ferroelectric behaviour. (e),(f) The in-plane direction perpendicular to the a-axis shows some signs of ferroelectric behaviour, but is mostly dielectric. [13].

FeFETs based on ferroelectric a/c domains instead of monodomains could differ considerably in function. Conventional FeFETs posses a up or down polarisation which modulate the resistance of the n-channel. The switching of the polarisation in either the up or down direction allows the switching between a high and low resistance state. In the case of the ferroelectric layer possesing multiple up or down polarised domains, the resistance can be switched over a wide range of intermediate states. As can be seen in Fig. 16, the polarisation behaviour of the a/c domains in strained $BaTiO_3$ is complex. The polarisation rotation causes the out-of-plane c-axis to rotate in-plane such that the $BaTiO_3$ layer is only ferroelectric in-plane along the a-axis. The polarisation rotation is the consequence of the twinning between the a/c domains leading to an in-plane flexoelectric field.
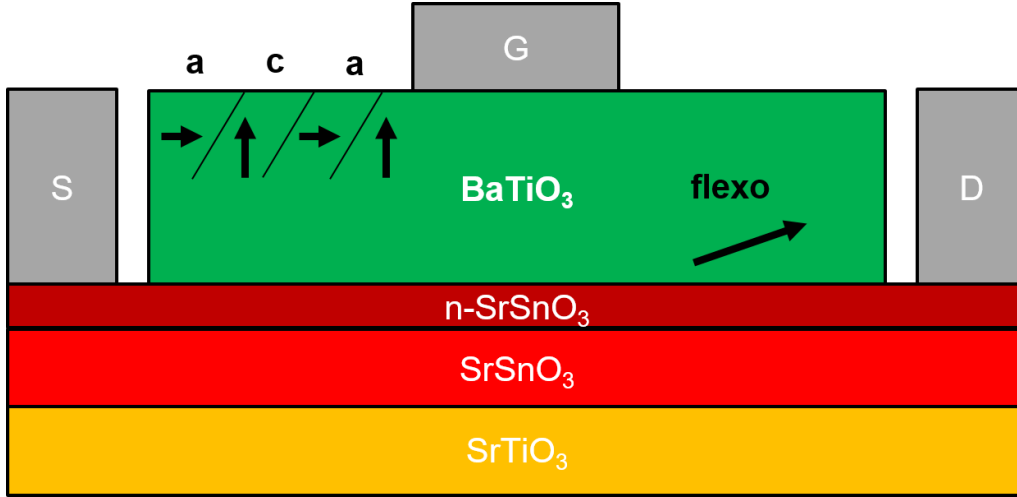

Figure 17: Ferroelectric field effect transistor incorporating novel ferroelectric phases $BaTiO_3$. The functionalities of the FeFET are shown: (S) source, (D) drain, (G) gate, $BaTiO_3$ as ferroelectric, n-$SrSNO_3$ as n-channel.

An schematic overview of the FeFET is given in Fig. 17, shown are the $SrTiO_3$ substrate and the $SrSnO_3$ spacer layer with an n-doped $SrSnO_3$ as n-channel layer. The $BaTiO_3$ layer possesses a/c domains and polarisation rotation is present due to the flexoelectric field caused by the twinning. If the polarisation rotation is not sufficiently strong enough to rotate the c-axis in-plane, then the $BaTiO_3$ film will posses an out-of-plane and in-plane polarisation caused by respectively the c and a domains. The polarisations of the a and c domains will have different polarisation time constants, thus the response of the a and c domains will differ for a time varying input signal. The time varying input signals could be pulse based in the context of implementing the spike-time-dependent plasticity (STDP) mechanism or sinusoidal for probing the memristive properties of the FeFET. The difference in polarisation time constants between the domains could possibly be exploited to create a short term memory and a long term memory. The short term memory with a small polarisation time constant could be used to add voltage pulses to enable polarisation switching in the long term memory. This mechanism would be reminiscent to the STDP mechanism. To verify the viability of this scheme, the polarization switching characteristics of strained $BaTiO_3$ grown on the $SrSnO_3$ film should be characterised. Furthermore the alternating perpendicularly oriented polarizations along the interface could create complex conduction behaviour along the interface between the source and the drain of the FeFET.

5 Methodology

This section gives a short discusion of the most prominent experimental techniques used during the master research project. The experimental techniques used served purposes ranging from fabrication to characterization. The fabrication techniques concern the deposition of thin films and electrodes, while the characterization techniques concern the determination of surface, structural and electrical properties. The doped $SrSnO_3$ and $BaTiO_3$ films are deposited using pulsed laser deposition (PLD). The surface characterisation is performed by using atomic force microscopy (AFM). A set of four different x-ray diffraction techniques is utilised, namely 2theta-omega scans, x-ray reflectometry, space mapping and rocking curve scans. The device fabrication is performed to deposit electrode contacts for two terminal and four terminal measurements. The two terminal measurements serve the purpose of characterising the conduction mechanisms through the $BaTiO_3$ layer. The four terminal measurements have the purpose of determining material properties such as resistivity, charge carrier density and charge carrier mobility. The following sections will discuss the above mentioned procedures and techniques in more detail.

5.1 Pulsed Laser Deposition

The films of $BaTiO_3$ and doped $SrSnO_3$ are grown using Pulsed Laser Deposition (PLD). This deposition technique relies on the deposition of material by laser ablation onto an heated substrate upon which the deposited material will either form islands or layers. The overview of the setup can be seen in Fig. 18. The PLD technique can be considered to involve two processes; material deposition by laser ablation and the film formation on the heated substrate. The formation of the film can be evaluated in situ by observing the Reflection High Energy Electron Diffraction (RHEED) pattern[13][14].
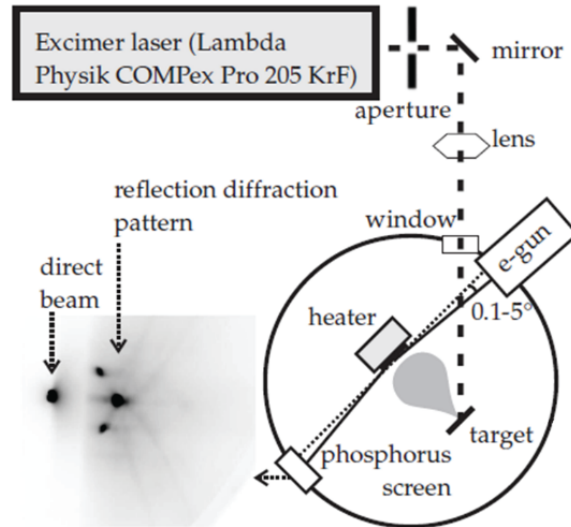

Figure 18: Pulsed Laser Deposition setup.

Growing perovskites with PLD requires control over the concentration of oxygen vacancies present in the film. The oxygen vacancies are controlled by applying a oxygen background pressure during the deposition. The applied oxygen background pressure vary over the range of 0.1mBar to 1mBar [33]. The mechanism of film growth is highly complex. The simplest model of film growth is the one for which atoms landing on the film select random sites at which they remain immobile, however for any finite temperature the atoms will diffuse over the surface until immobilised by an energetically favourable site. Moreover the particles in the plume are not neutral atoms, but a variation of charged and neutral clusters of atoms [34].

19

In the case of a defect free surface with stepped terraces, as is the case for HBF treated $SrTiO_3$ substrates, the adatoms will immobilize by incorporation at the step edge and form islands when two adatoms meet[35]. The resulting film growth modes can be divided in four categories; layer-by-layer or Frank van der Merwe growth, Volmer-Weber growth, Stranski-Krastanov and step-flow growth. The film growth mode can be determined by monitoring the RHEED signal. The intensity of the RHEED signal will vary depending on the filling of the layer; complete filling will lead to an maximal intensity of the signal, while half filling leads to a minimum. The layer-by-layer growth modes will lead to oscillations in the intensity of the RHEED signal, while for island growth modes the RHEED signal will decrease or remain constant[36].

5.2 Atomic Force Microscopy

Atomic force microscopy (AFM) has been used to study the surface of the films and substrate to obtain topographical data and find indications of difference in chemical composition. This data is obtained by using AFM tapping mode[37]. The general operating principles of an AFM setups consist of scanning a tip from a cantilever over an sample surface with feedback mechanisms ensuring a constant force or height between the sample and the tip, see Fig. 19. As the tip scans the surface, the cantilever will move up and down. The movement of the cantilever is measured by the deflection of the laser from the back of the cantilever. The reflected laser light hits an position sensitive detector. The position sensitive detector consists of four quadrants, deflection of the laser light results in shifts of the light intensity in each quadrant. The intensity shifts can be used to determine the lateral and perpendicular displacement of the tip. The feedback mechanisms will then use the displacement of the cantilever to keep the tip at constant height or force.

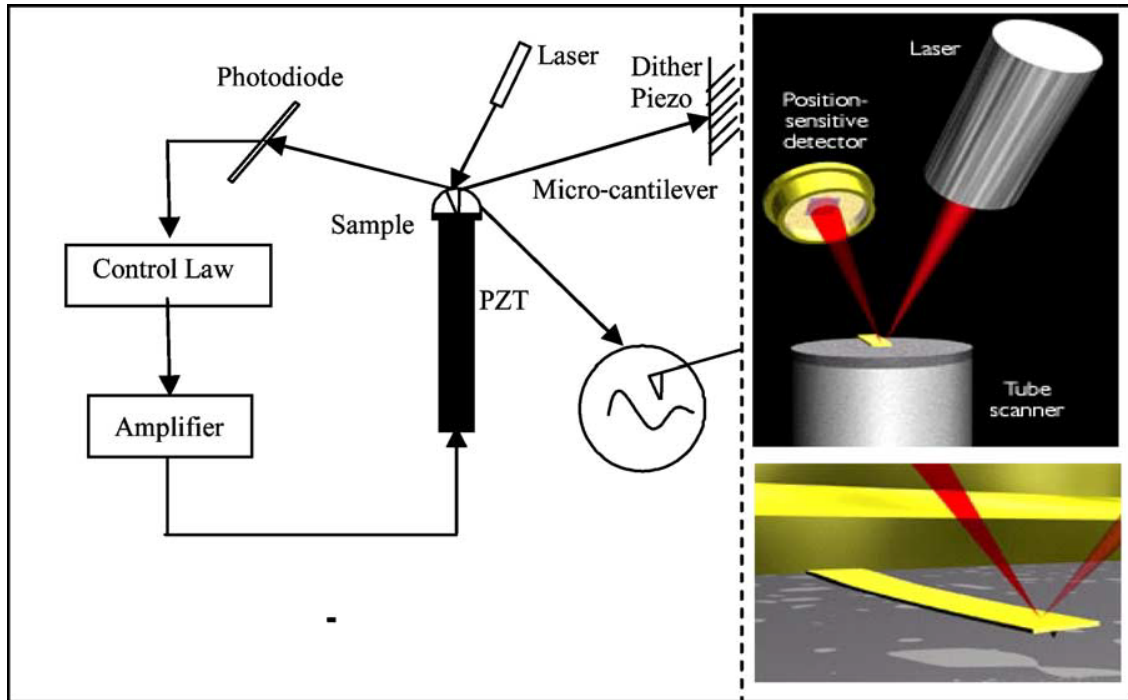Figure 19: Basics of atomic force microscopy (AFM) system. On the left side the cantilever position dependent feedback system is depicted. Furthermore the piezo elements controlling the sample and cantilever position are shown. Upper right corner shows the laser being reflected from the cantilever on the position sensitive detector. Lower right corner shows the cantilever and tip above the sample surface[38].

The general operating principles are valid for the three commonly encountered operating modes, these operating modes are non-contact mode, contact mode and tapping mode. The AFM measurements performed during the master research project are done in AFM tapping mode. In AFM tapping mode the cantilever is oscillated near its natural resonant frequency using a piezoelectric actuator. The piezoelectric actuator applies a force at the base of the cantilever and the oscillating tip is moved to the surface of the sample. The vibrating tip will touch the sample and oscillate with reduced amplitude. The tip-surface interactions effects the amplitude and phase of the oscillating cantilever. The adjustment of the z-position to keep the cantilever oscillating at constant amplitude is depicted in the height image. Phase shifts near the resonance frequency of the cantilever are pronounced and can be measured independently of height [39]. The result is two main channels for operating AFM in tapping mode, namely the phase channel and the height channel. These two channels can be used to characterise the surface properties of the $SrTiO_3$ substrate and the $SrSnO_3$ and $BaTiO_3$ films.

The height and phase channel provide different types of surface information. The height channel provides information over the surface topography such as the height profile and surface roughness. The phase channel provides information over difference in material composition. As example can be considered the sonification of an (100) oriented $SrTiO_3$ sample in water, the sample posses a miscut angle such that the flat surface consists of alternating SrO or TiO_2 terminated regions. During sonification in demineralised water the H_2O binds to the SrO, the chemical composition between the SrO and TiO_2 differs such that a major difference in phase is present, see Fig. 20.

(a) Height image tapping mode AFM of annealed $SrTiO_3$ after water sonification.

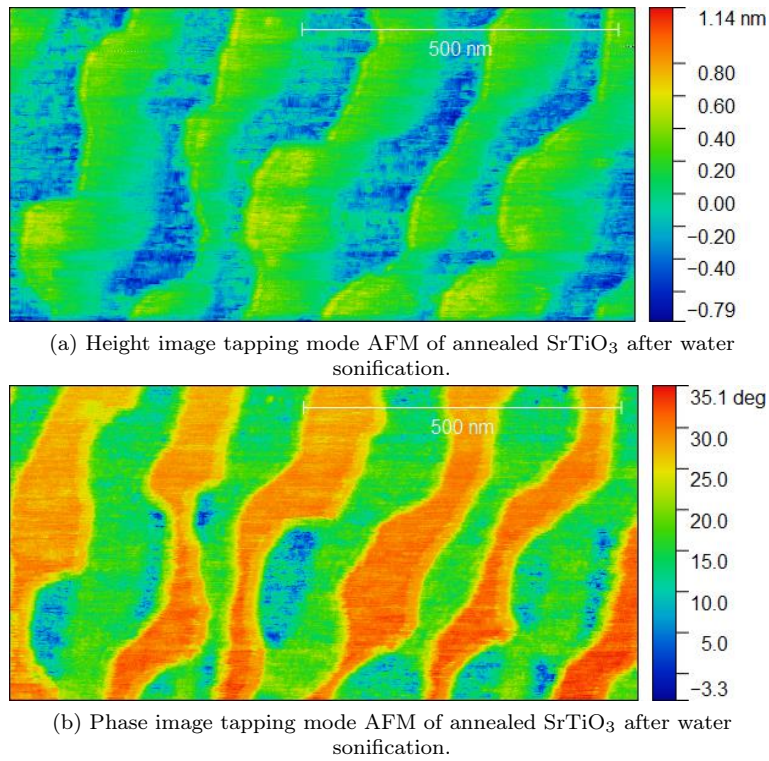(b) Phase image tapping mode AFM of annealed $SrTiO_3$ after water sonification.

Figure 20

5.3 X-ray diffraction techniques

The structure of the grown films are characterised by the use of x-ray diffraction techniques. X-ray diffraction techniques allow the non-destructive characterisation of the crystal structure post growth. Four different x-ray diffraction techniques are utilised, each focused on characterising different aspects of the strained and epitaxially grown films. These techniques are 2theta-omega, reflectometry, space maps and rocking curve scans. The following sections will explain the working principles behind these techniques and show what kind of structural information can be obtained using these techniques.
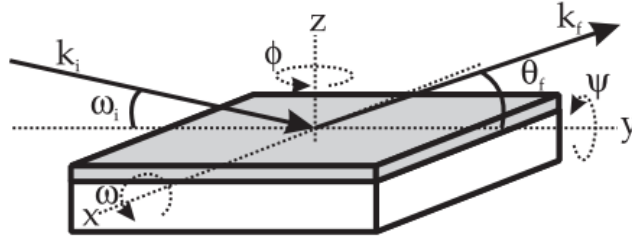

Figure 21: X-ray diffraction angles. ω_i is the incidence angle and θ_f the outgoing angle.[14]

5.3.1 2Theta-Omega Scans

The structural characterisation of the grown thin films starts with the determination of the crystal structures and orientations in conjecture with literature. The 2theta-omega scans are used to determine these properties. The 2theta-omega scans are performed by measuring the intensity over the range of the 2theta angle. Diffraction peaks are encountered under constructive interference, as given by Braggs law:

$$n\lambda = 2d_{hkl}sin(\theta_{hkl}) \tag{12}$$

with $n\lambda$ being an integer amount of x-ray wavelengths, d_{hkl} being spacing of the crystal planes and θ the angle of incidence between the incoming x-ray and crystal plane. The positions of the diffraction peaks can give information over the reflection conditions and orientation of the film, allowing the determination of the lattice parameters of the found crystal unit cells.

5.3.2 Reflectometry

Information over layer thickness, density and roughness can be obtained from x-ray reflectrometry[40]. Reflectometry measurements are performed by measuring the intensity of the reflection from the x-ray incident on the sample from an angle of 0.5 to 5 degrees. The reflected intensity depends on the thickness d, electronic density ρ, the interface roughness σ and the x-ray wavelength k. In the case a single film is deposited on a substrate, the reflected intensity is:

$$R = |r|^2 = |\frac{\tilde{r}_{01} + \tilde{r}_{12}p^2}{1 + \tilde{r}_{01}\tilde{r}_{12}p^2}|^2 \tag{13}$$

$$\tilde{r}_{ij} = r_{ij}exp(-\frac{k^2\sigma_j^2 sin(\alpha_i)sin(\alpha_j)}{2}) \tag{14}$$

$$r_{ij} = \frac{\alpha_i - \alpha_j}{\alpha_i + \alpha_j} \tag{15}$$

where the angles α_i and α_j are related to the refractive index n through the generalized Snell equation:

$$n_i cos(\alpha_i) = n_j cos(\alpha_j) \tag{16}$$

The phase factor p^2 leads to the formation of Kiessig fringes:

$$p^2 = exp(i2ksin(\alpha)d) \tag{17}$$

The periodicity of the Kiessig fringes is inversely proportional to the film thicknes according to d = k/2 $\Delta\alpha$ with $\Delta\alpha$ is the difference in angular position between two maxima or minima. Below the critical angle the x-rays are totally reflected and no periodicity is present, the critical angle depends on the electronic density according to $\alpha_{crit} = \sqrt{4\pi\rho r_0/k^2}$. More complex situations involving two or more films being deposited on a substrate can be solved analytically by computer simulations. To fit the x-ray reflectometry data obtained during the master research project the fitting program GenX3 is used.

5.3.3   Reciprocal Space Mapping

To study the strain relaxation and the epitaxy of the growth reciprocal space maps can be used[40]. Reciprocal space maps are performed by recording 2θ-ω scans for a range of different ω values producing a 2D reciprocal space map. The measurements in angle space can be converted to reciprocal k-space. The units in k-space are measured in units of Ewald's sphere diameter $4\pi/\lambda$. To compare reciprocal space maps for different substrates, normalization with respect to the substrate lattice parameter a_{sub} gives q-space. The transformation from angle space to q-space is thus given by:

$$q_\perp = \frac{2a_{sub}}{\lambda}sin(\theta) \cdot cos(\omega - \theta) \tag{18}$$

$$q_{||} = \frac{2a_{sub}}{\lambda}sin(\theta) \cdot sin(\omega - \theta) \tag{19}$$

After the conversion of the angle data to q-space, the reciprocal space maps are converted to non-reciprocal space maps. The transformation of reciprocal to real space involves inversion. To plot the real space as a grid Akima interpolation is used[41]. The Akima method uses a piecewise function composed of a set of polynomials with a maximal degree of three. The result being a smooth space map in real space.

5.3.4   Rocking Curve Scans

Rocking curve scans are obtained by varying the omega angle while the 2-theta angle is fixed[42]. The 2-theta angle is set at an diffraction peak position, while the omega angle is varied over a few degrees around the 2-theta angle. The rocking motion produces a rocking curve which can be analysed to study the mosaicity of the film. Mosaicity describes the angular distribution of the crystal planes out-plane of the film. The mosaicity is the consequence of the formation of dislocations in a strained film above a critical thickness[?]. The mosaicity is noticed by the rocking curve deviating from the ideal case of fully out-plane oriented crystal planes. The ideal case consists of the rocking curve possesing a full width half maximum (FWHM) solely due to instrumental broadening of the diffraction peak. This ideal case is described by the Lorentzian distribution given by:

$$I = \frac{1}{\pi\gamma}\left[\frac{\gamma^2}{(\omega - \omega_0)^2 + \gamma^2}\right] \tag{20}$$

where 2γ is the scale parameter describing the FWHM and ω_0=2θ, while ω is the varied angle. The presence of dislocations and mosaicity can thus be discussed by deviations of the experimental intensity distribution from the ideal Lorentzian distribution.

5.4 Electrical Measurements

The electrical measurements have been performed to characterise various phyiscal properties of doped $SrSnO_3$ and $BaTiO_3$ films. The electrical measurements can be divided in two terminal and four terminal measurements. The fabrication of electrodes on the samples is done by using UV-photolithography, reactive ion beam etching and sputtering. The following section will describe the fabrication of the electrodes on the samples. Furthermore the measurements done in the two and four terminal setup will be explained.

5.4.1 Device Fabrication

To perform electrical measurements on the PLD grown samples it is necessary to fabricate electrodes on the samples. To fabricate electrodes UV-photolithography, reactive ion beam etching and sputtering is used. The UV-lithography technique is used to develop electrodes on the top film of the grown sample. Reactive ion beam etching is used to contact the bottom layer of multi-layer PLD grown samples. The electrode material is deposited using sputtering[43].

The UV-photolithography technique is used to develop patterns on metal and semi-conductor surfaces. Possible patterns include electrode contacts. The following steps are undertaken to develop electrode contacts on the grown films. First the samples are spincoated with photoresist. The spin coated samples are then prebaked at 110C to harden the photoresist. Subsequently the mask with the pattern of electrode contacts is placed over the sample and the substrate with photoresist is exposed to ultra violet (UV) light. The use of UV light with an wavelength of roughly 400nm allows the fabrication of patterns with an resolution of 1 μm. A negative photoresist is used, which hardens upon exposure to UV light. The sample is post baked after exposure to evaporate solvent. The postbaked sample is treated with an developer to remove the hardened photoresist. The pattern left behind consist of photoresist covering the majority of the samples with photoresist free parts for future electrodes. The electrodes are deposited using sputtering, after sputtering the whole sample surface is covered by the sputtered metal. The photoresist is lifted off by the use of acetone, which also removes the sputtered electrode material on top of the photoresist. The end result is an sample with only sputtered metal left behind at the place of the electrodes.

Sputtering is a technique in which chunks of atoms are knocked out of a target acting as an electrode upon a substrate acting as another electrode. The setup works as follows, the target and substrate functioning as electrodes are faced opposite to each other in the chamber of the sputtering machine. In the chamber Ar is present as an inert gas under a pressure of 100 mtorr. The Ar is used to initiate and maintain a discharge. An electric field is applied between the target and substrate by a DC voltage. The target is the cathode and the substrate is the anode. The free electrons accelerate from the cathode to the anode and ionise the Ar atoms. The positively charged Ar atoms accelerate to the cathode ejecting chunks of atoms from the target. The neutral and negative target atoms pass through the discharge and hit the anode. The deposited atoms will form a film on the substrate. This technique is used to deposit the Ti electrodes on the samples. The Ti electrodes are protected by an Pt layer deposited over the Ti as an protection against oxidation.

The reactive ion beam etching shares similarities with the sputtering technique. However no chunks of atoms are ejected from the target to form a film on the substrate. The electric field between the cathode and anode is used to accelerate the free electrons into the gas between the cathode and anode. The gas is ionized into highly reactive components, a possible gas is CH_3F. The reactive components of the ionized gas get accelerate to the substrate and etch the surface. The reactive ion beam etching is utilised to contact the $SrSnO_3$ film underneath the $BaTiO_3$ film for electrode deposition. The electrode deposition works as follows. The samples are protected by an hard mask with holes at the place for the electrodes, the sample will only be etched at the exposed parts. The hard mask is left on after the etching and the sample is sputtered with

electrodes. After the electrode deposition, the hard mask is removed and the SrSnO$_3$ contacting electrodes are ready for electrical measurements.

5.4.2 Two terminal measurements

The two terminal measurements are performed on Ti/BaTiO$_3$/Y$_{0.05}$Sr$_{0.95}$SnO$_3$ samples. These samples consist of an Ti electrode on a BaTiO$_3$ film grown under strain on a Y$_{0.05}$Sr$_{0.95}$SnO$_3$ film. The Y$_{0.05}$Sr$_{0.95}$SnO$_3$ film itself is deposited on an SrTiO$_3$ substrate. The Y$_{0.05}$Sr$_{0.95}$SnO$_3$ film is contacted using reactive ion beam etching and electrodes are deposited on the Y$_{0.05}$Sr$_{0.95}$SnO$_3$ film. The measurements over the Ti/BaTiO$_3$/Y$_{0.05}$Sr$_{0.95}$SnO$_3$ stack gives information over the the conductivity through the BaTiO3 and the role of the Ti:BaTiO$_3$ and Y$_{0.05}$Sr$_{0.95}$SnO$_3$:BaTiO$_3$ interfaces. These characteristics can be determined using temperature dependent current-voltage sweeps.
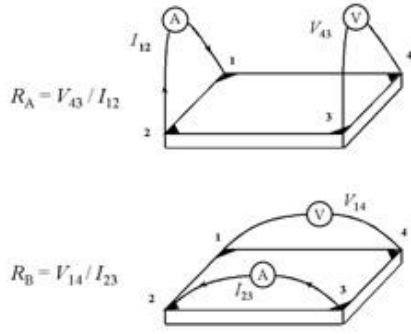
(a) Electrical contacts setup Van der Pauw measurements.
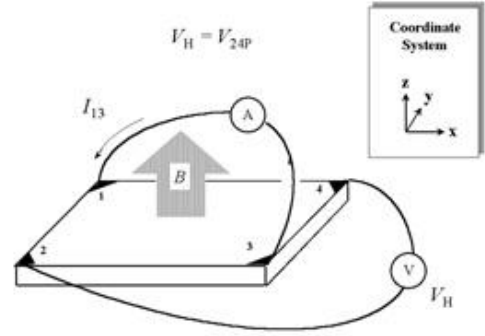
(b) Electrical contacts setup Hall measurements.

Figure 22

5.4.3 Four terminal measurements

The four terminal measurements are performed over a temperature range of 5K to 400K, the specific measurements performed are the Van der Pauw measurements and the Hall measurements[44][45]. The goal of the four terminal measurements is to determine physical properties of thin SrSnO$_3$ films. The Van der Pauw and Hall measurements are performed on samples with a square geometry with contacts deposited at the corners. This geometry is acceptable for Van der Pauw measurements, but for doing Hall measurements a bridge-type sample geometry is more likely to give accurate results.

The van der Pauw technique is used to determine the sheet resistance R_S from which the bulk electrical resistivity can be determined by:

$$\rho = R_S d \tag{21}$$

with ρ the bulk electrical resistivity and d the film thickness. The voltage is sourced over the contacts opposing the contacts over which the current is measured giving the sheet resistances R_A and R_B, as can be seen in Fig. 22. The sheet resistance R_S can be determined using the van der Pauw equation:

$$e^{-\pi R_A/R_S} + e^{-\pi R_B/R_S} = 1 \tag{22}$$

The van der Pauw equation can be solved analytically using the Newton-Raphson method. The relative error in the measured resistance are on the order of the ratio between the diameter of the electrical contact and the distance between the contacts.

The Hall measurements have the objective to determine the sheet charge carrier density n_s. This is done by the measuring of the Hall voltage V_H. The Hall voltage measurement consists of determining the Hall voltage perpendicular to the current flow I under an applied magnetic field B, see Fig. 22. The sheet charge carrier density is then determined using:

$$n_S = \frac{IB}{eV_H} \tag{23}$$

Based on the found sheet resistances and charge carrier density, it is possible to determine the charge carrier mobility using:

$$\mu = \frac{1}{en_S R_S} \tag{24}$$

To summarise, the four terminal measurements allow the determination of resistivity, charge carrier density and charge carrier mobility in thin films.

6 Nb doping of SrSnO$_3$

The goal of the PhD project related to my master research project is to find novel ferroelectric phases in strain engineered BaTiO$_3$. The BaTiO$_3$ is strained by an SrSnO$_3$ film grown on a SrTiO$_3$ substrate. The strain of the SrSnO$_3$ on the BaTiO$_3$ is tuned by doping the SrSnO$_3$ to tune its lattice parameter. In case of the successful strain engineering of novel ferroelectric phases, the next step is to study the memristive properties of such system. The end goal is to create a memristive device by integration of the strain engineered BaTiO$_3$ into an ferroelectric field effect transistor (FeFET). To create an effective FeFET, it is important to have an highly conductive n-channel. The n-channel can be by growing a thin film of n-doped SrSnO$_3$ on the strain engineered SrSnO$_3$ film. The n-doped SrSnO$_3$ must have good epitaxy with the underlying SrSnO$_3$ film and grow with low surface roughness to ensure the BaTiO$_3$ will still have the appropriate strain.

6.1 Choice of doping

Doping SrSnO$_3$ is an popular subject of research, a significant amount of papers has been written utilizing a wide range of dopants and substrates. The most interesting dopant is La due to the high electron mobility's measured well in excess of 25 cm^{2}V^{-1}s^{-1} for substrates such as SrTiO$_3$, NdScO$_3$ and GdScO$_3$ [46][47]. The high electron mobility is caused by the La substituting the Sr. The La has an larger ionic radius than Sr resulting in a decrease of the tilting of the oxygen octahedra in the perovksite crystal unit cell. The consequence is an increase of the lattice parameter of the La doped SrSnO$_3$ [48]. The increased lattice parmater leads to issues with the strain on the BaTiO$_3$ film. The reason is that the novel ferroelectric phases can only emerge when the lattice parameter (a=4.04 Å) of the orthorhombic (nearly cubic) SrSnO$_3$ lays in between the a (3.99 Å) and c (4.03 Å)-lattice parameter of the tetragonal BaTiO$_3$. The undoped SrSnO$_3$ has a lattice parameter slightly larger than the c lattice parameter of BaTiO$_3$, so n-doping SrSnO$_3$ with La is not viable in the context of strain engineered ferroelectric phases.

The ideal n-doped SrSnO$_3$ film has an lattice parameter between the a and c lattice parameter of BaTiO$_3$. Considering that the n-doped SrSnO$_3$ will be grown on top of strained SrSnO$_3$, n dopants which do not significantly change the lattice parameter of SrSnO$_3$ could also be considered. A suitable dopant fullfilling these requirements will be Nb. The Nb dopes the Sn site, the Sn sites are the centres of the oxygen octahedra which shield the Sn site limiting the effects of the dopant on the lattice parameter. The limited effect on the lattice parameter has been shown in computational studies [49] and the Nb doping the Sn site has been experimentally verified by x-ray photon spectroscopy measurements for both SrSnO_3 and BaSnO$_3$[50][51]. The Nb acts as an pentavalent dopant [51][50] with the most favourable charge compensation mechanisms being Sr antisite defects and Sn vacancies[49], currently the existence of Sr antisite defects and Sn vacancies has not been verified by electron microscopy measurements. Furthermore the optimal Nb doping of SrSnO$_3$ is Nb:Sn of 5:95, or SrNb$_{0.05}$Sn$_{0.95}$O$_3$[50].

6.2 Fabrication

The SrNb$_{0.05}$Sn$_{0.95}$O$_3$ target for Pulsed Laser Deposition is fabricated using conventional solid-state reactions [50] [52] using $SrCO_3$, SnO_2 and Nb_2O_5 as raw materials. These raw materials were grinded and pressed for three sounds of sintering. The first round of sintering is performed by heating the target to 1225C in 4h, keeping the temperature for 12h followed by uncontrolled cooling to room temperature. The second round of sintering is performed by heating the target to 1300C in 4h, keeping the temperature for 12h and cool to 30C over 12h. The third and last round of sintering consisted of heating the target in 3h to 1400C, keeping the temperature for 10h and cool to 30C over 12h. After the sintering the target is glued to an holder and used for Pulsed Laser Deposition.

6.3   Growth optimization

After the fabrication of the $SrNb_{0.05}Sn_{0.95}O_3$ target, the growth of the films using Pulsed Laser Deposition (PLD) still has to be optimized. An oxygen pressure of 0.3mBar leads to good results for Y and Ti doped $SrSnO_3$ films, it is assumed that this oxygen pressure is also optimal for Nb doped $SrSnO_3$ films. The laser fluency will also have an impact on the growth rate of material in a certain time interval. The growth is controlled using Pulsed Laser Interval Deposition(PLID). An initial film is deposited using 1Hz laser pulses at an pulse energy of 35±0.2 mJ. The film thickness is then determined using x-ray reflectometry and the amount of pulses per layer is calculated. The PLID recipe will fire the amount of pulses needed per layer in 1s, after which the deposited material will diffuse over the surface for a period of 8-12s. Misalignment of the target with respect to the substrate will lead to differences in thickness of the deposited films or, in extreme cases, difference in stochiometry. The deposition temperature is an critical parameter for the growth of thin films as it determines the film formation dynamics during deposition. Due to the suboptimal surface quality of the Nb doped $SrSnO_3$ films at 650C, it is decided to vary the temperature between growths with the goal of finding the optimal deposition temperature for $SrNb_{0.05}Sn_{0.95}O_3$ thin films.
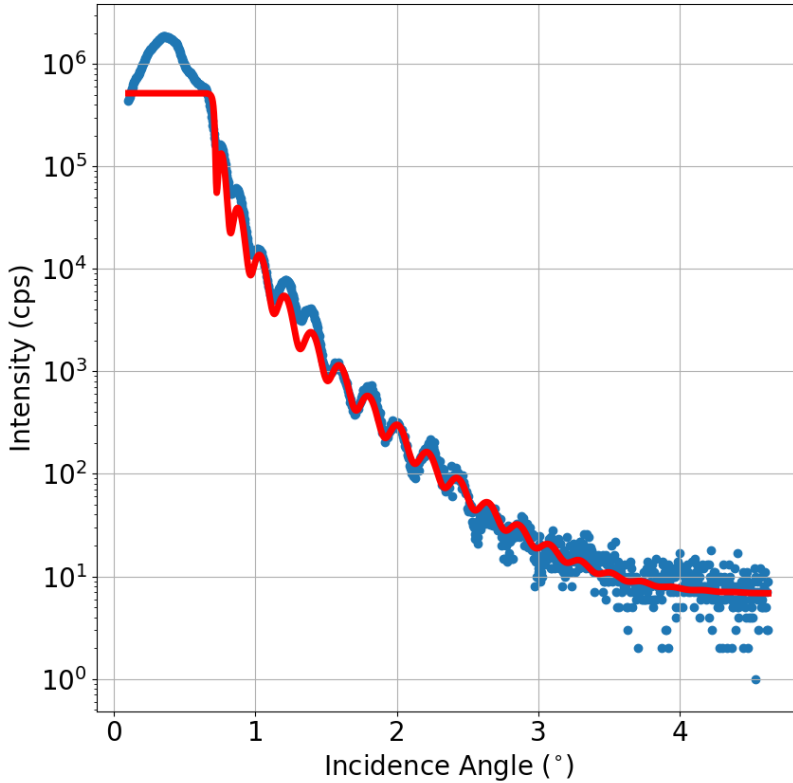

Figure 23: X-ray reflectometry scan of the $SrNb_{0.05}Sn_{0.95}O_3$ film deposited at 650C. The film thickness is 39.6±1 nm, roughly 100 $SrSnO_3$ unit cells thick. The electron density at 0.5∘ is abnormal and not present in the x-ray reflectometry scans of other $SrNb_{0.05}Sn_{0.95}O_3$ films.

The $SrNb_{0.05}Sn_{0.95}O_3$ thin films have been grown for four different deposition temperatures; namely 550C, 600C, 650C and 700C. The film thicknesses are verified using x-ray reflectometry, see table 1. The surface of the deposited films have been characterized using tapping mode AFM.

The structural characterization has been performed using 2theta-omega scans, space maps and rocking curve scans. The goal of the surface and structural characterization is to determine the optimal deposition temperature by analyzing the surface quality and the strain relaxation. First the surface quality will be discussed, secondly the structural characterization are analyzed using x-ray diffraction techniques.

Deposition temperature(C)	Film thickness (nm)
550	49.0$\pm$1
600	49.3$\pm$1
650*	39.6$\pm$1
700	50.2$\pm$1

Table 1: Film thickness $SrNb_{0.05}Sn_{0.95}O_3$ for different deposition temperatures. *(Sample deposited before laser realignment, different PLID recipe)

6.4 Surface quality

The AFM imaging yields surprising results. The standard PLD growth recipes for doped and un-doped $SrSnO_3$ films show minimal surface roughness at a deposition temperature of 650C, however the results for $SrNb_{0.05}Sn_{0.95}O_3$ films are considerably different. The film deposited at 650C shows considerable island growth. The islands on the film are roughly 20nm high, the height of the islands is roughly 75% of the film thickness. The surface between the islands has a root mean square roughness of 1.179nm. For a lattice parameter of 0.4nm is the height variation across the surface three unit cells, far from atomically flat. Assuming that the PLID recipe is accurate enough for layer-by-layer growth, the reason of poor surface quality can be attributed to sub-optimal growth dynamics due to sub-optimal deposition temperature. To research this possibility, three more films at different temperatures, namely 550C, 600C and 700C.
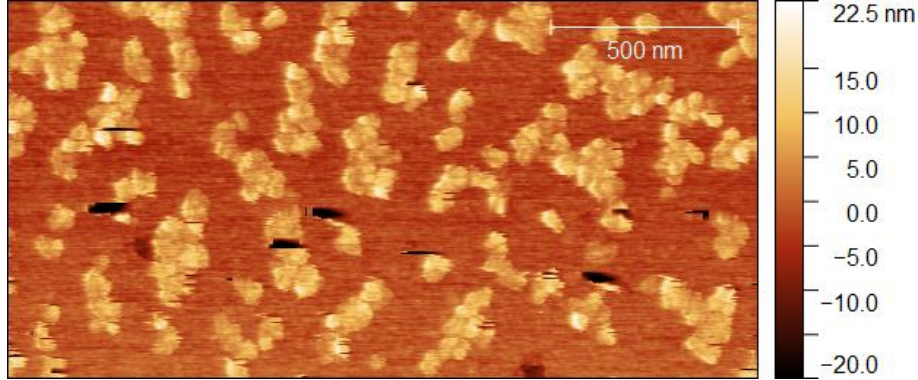

Figure 24: Surface of $SrNb_{0.05}Sn_{0.95}O_3$ film for deposition temperature of 650C. A large amount of island growth is present, between the islands the mean square roughness is 1.179nm.

The $SrNb_{0.05}Sn_{0.95}O_3$ film deposited at 5500C shows a very interesting surface texture. The film has an very grainy surface, the grains range in size from 10-60nm, furthermore islands from 5nm high are present across the film surface, see Fig. 25. However the most interesting feature present is that the grain boundaries are higher than most of the grains themselves. The phase image shows a clear difference in phase between the grains and the grain boundaries, indicating a difference in material. The difference in material can be caused by either crystalline or amorphous grain boundaries. The absence of additional peaks in the 2theta-omega scan suggests amorphous grain boundaries, see Fig. 29. The $SrNb_{0.05}Sn_{0.95}O_3$ film deposited at 550C is unsuitable for growing $BaTiO_3$ under epitaxial strain, so 550C is not the right deposition temperature for using $SrNb_{0.05}Sn_{0.95}O_3$ as an n-channel material.
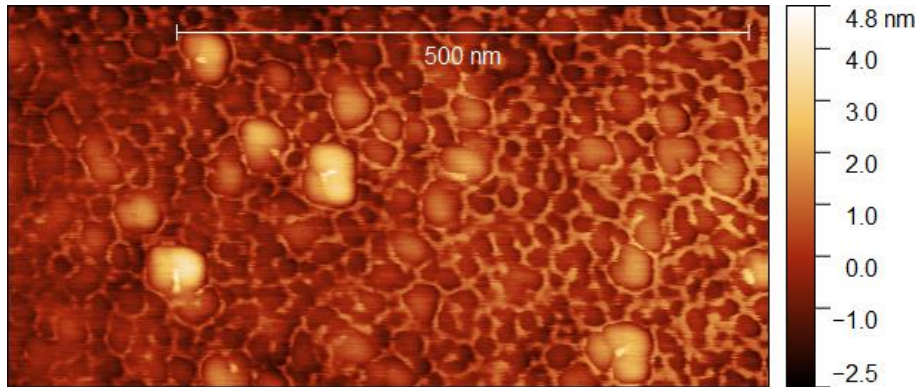

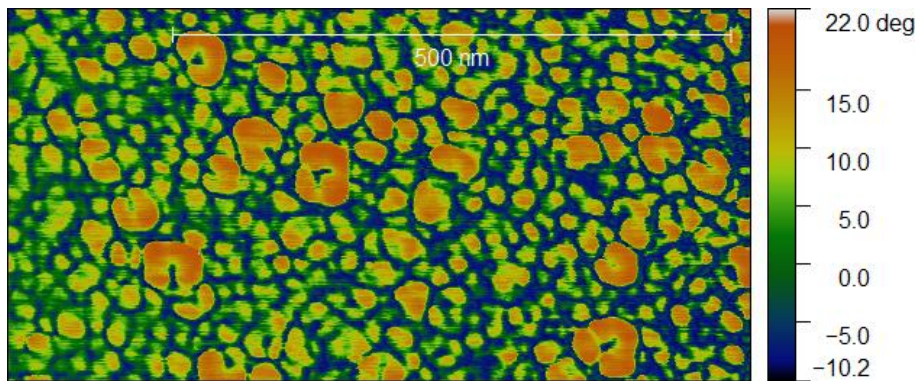Figure 25: Height image of NbSSO film for deposition temperature of 550C. Root mean square roughness is 732pm.

Figure 26: Phase image of NbSSO film for deposition temperature of 550C.

$SrNb_{0.05}Sn_{0.95}O_3$ films have also been deposited at 600C and 700C from both of these films AFM images have been made, see Fig. 27 and Fig. 28. The film grown at 600C is considerably smoother than the film grown at either 650C or 700C. The 600C film has an root mean square roughness of 525.8 pm, while the films grown at 650C and 700C have a mean square roughness of respectively 1.179nm and 0.923nm. Interesting to note is that the island height and surface roughness at 650C and 700C is roughly comparable, but at 700C the island start to orient themselves in lines a terrace width apart. Although the 600C film has some 4nm island growth, the overall smoothness of the film approaches that of a $SrSnO_3$ unit cell. The AFM images imply that only at 600C smooth $SrNb_{0.05}Sn_{0.95}O_3$ films can be deposited well enough for use as an n-channel layer.
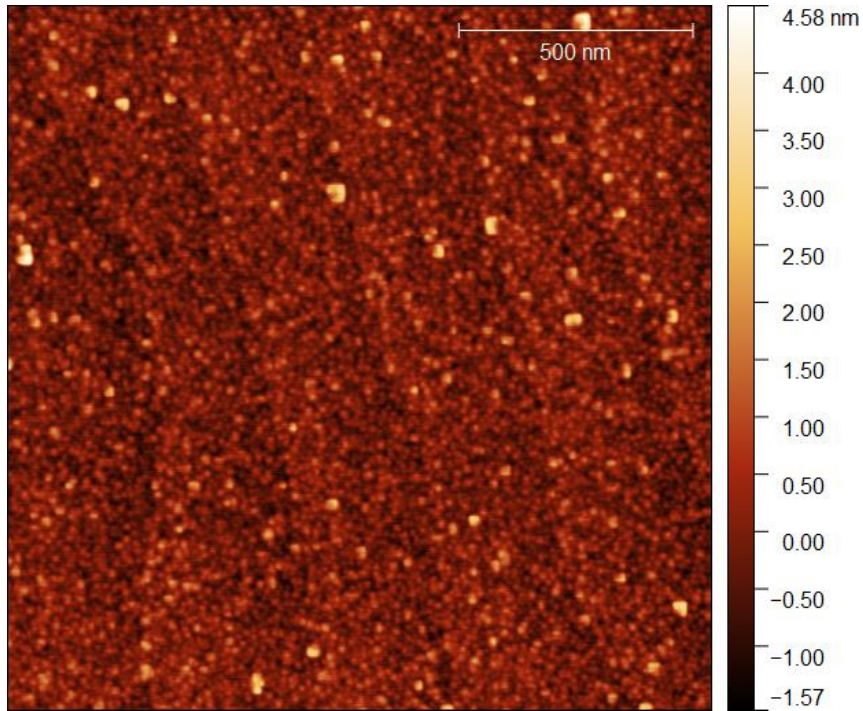
Figure 27: Surface of $SrNb_{0.05}Sn_{0.95}O_3$ film deposited at 600C. The root mean square roughness is 525.8pm.
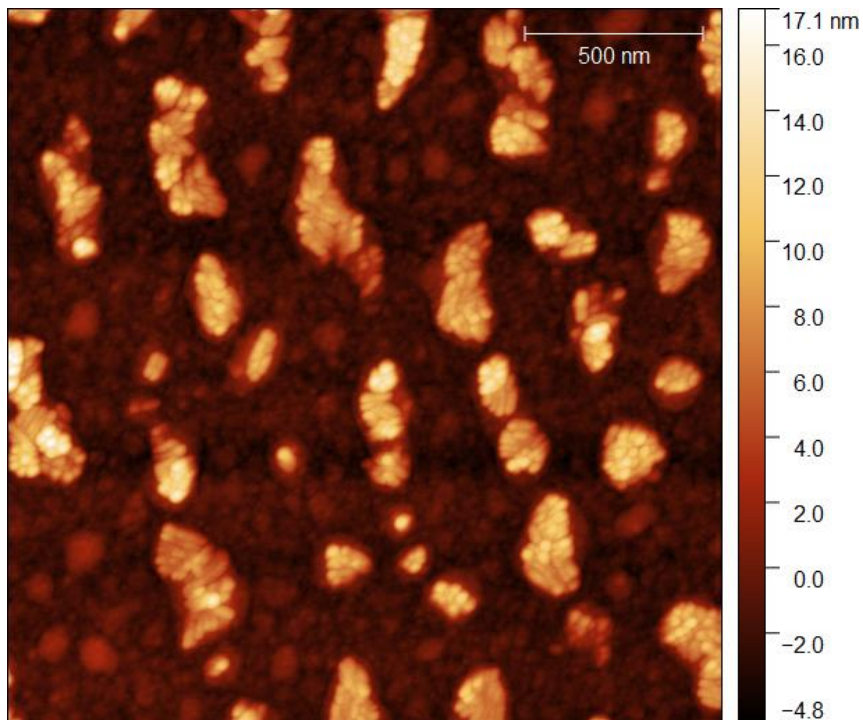

Figure 28: Surface of $SrNb_{0.05}Sn_{0.95}O_3$ film deposited at 700C. The deposited film shows island growth of 17nm with a root mean square roughness of 923.0 pm in between the islands.

6.5 Structural characterization

The goal of the structural characterization is to observe the crystallinity, epitaxy and strain relaxation of the grown films for different temperatures. At the right deposition temperature the $SrNb_{0.05}Sn_{0.95}O_3$ should grow with a (001) orientation and the lattice parameters should be smaller or comparable to undoped $SrSnO_3$. To study the structural properties three different x-ray techniques have been used; 2theta-omega scans, space maps and rocking curve scans.

The 2theta-omega scans do not differ significantly between the films deposited at different temperature. The peaks present can all be contributed to the (100) diffraction peaks of $SrTiO_3$ and $SrSnO_3$, see Fig. 29. There are no additional peaks present in any of the films implying that the crystalline film is (100) oriented. More interesting behaviour can be seen when studying the epitaxy and strain relaxation.
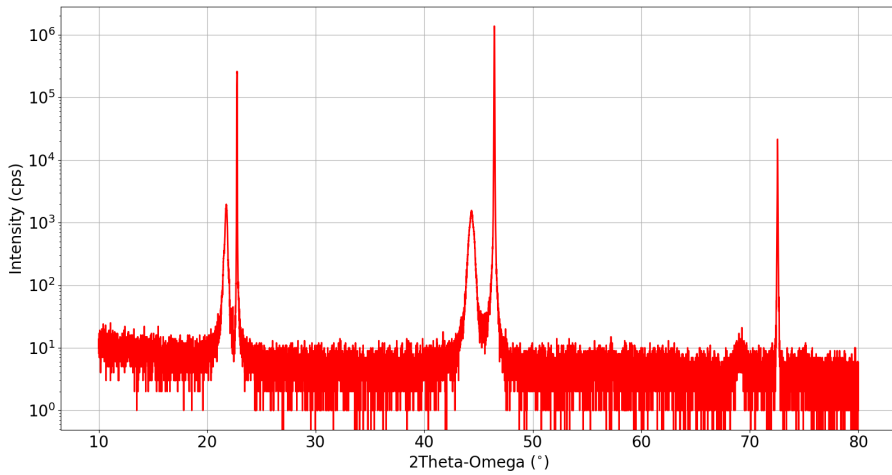

Figure 29: 2Theta-Omega scan for $SrNb_{0.05}Sn_{0.95}O_3$ film deposited at 550C.

The epitaxy and strain relaxation can be studied using space maps and rocking curve scans. The space maps have been performed around the (103) peak of both the $SrTiO_3$ and $SrSnO_3$ to study the in-plane and out-plane strain relaxation. The rocking curve scans have been performed around the (200) peak of $SrSnO_3$, performing rocking curves around the (100) peak of $SrSnO_3$ leads to a contribution to the intensity by the (100) peak of the $SrTiO_3$. Interesting to note is the similarity of the space map and rocking curve scan for the $SrNb_{0.05}Sn_{0.95}O_3$ film deposited at 550C and 600C, the lattice parameters and FWHM are nearly the same, see Fig. 30 and Fig. 31. This is surprising due to the film surfaces differing significantly, the 550C film has a complex grainy surface showing no terrace features, while the 600C surface shows a well-defined film with terrace features still present. Compared to the bulk lattice parameters (a=c=4.04Å), the films seem to be compressed in the in-plane (a 4.01Å) direction and extended in the out-plane dirrection (c 4.08Å). Although the $SrNb_{0.05}Sn_{0.95}O_3$ film is strained, the growth is not epitaxial. Fitting the Lorentzians to the rocking curves indicates that the tails are to pronounced for fitting, a possible reason could be some minor strain relaxation from lattice parameters close to the $SrTiO_3$ substrate to lattice parameters close to the $SrSnO_3$ bulk. The $SrNb_{0.05}Sn_{0.95}O_3$ film deposited at 650C seems to consist of two conjoined regions, in one region the lattice parameters are larger than bulk (a 4.12Å) and in the other region the lattice parameter is close to the substrate parameter (a 3.92Å), see Fig. 32. The region of 4.12Åto 3.92Åhas an almost constant intensity, indicating a large variance in lattice parameters. Separating the regions and studying the strain relaxation seems impossible. The rocking curve for the 650C film is poorly defined due to the large distribution

of lattice parameters, as indicated by the low intensity and large FWHM. The x-ray data for the 700C film has an closer resemblance to the films deposited at 550C and 600C than 650C, see Fig. 33, the cause could possibly that the 650C film is 10nm thinner than the other films. The film deposited at 700C shows a compressed in-plane parameter (a 4.01Å) and an extended out-plane parameter (c 4.07Å). The rocking curve has an FWHM an order of magnitude larger than the FWHM of the 550C and 600C film, so a larger variance in the distribution of lattice parameters seems to be present.
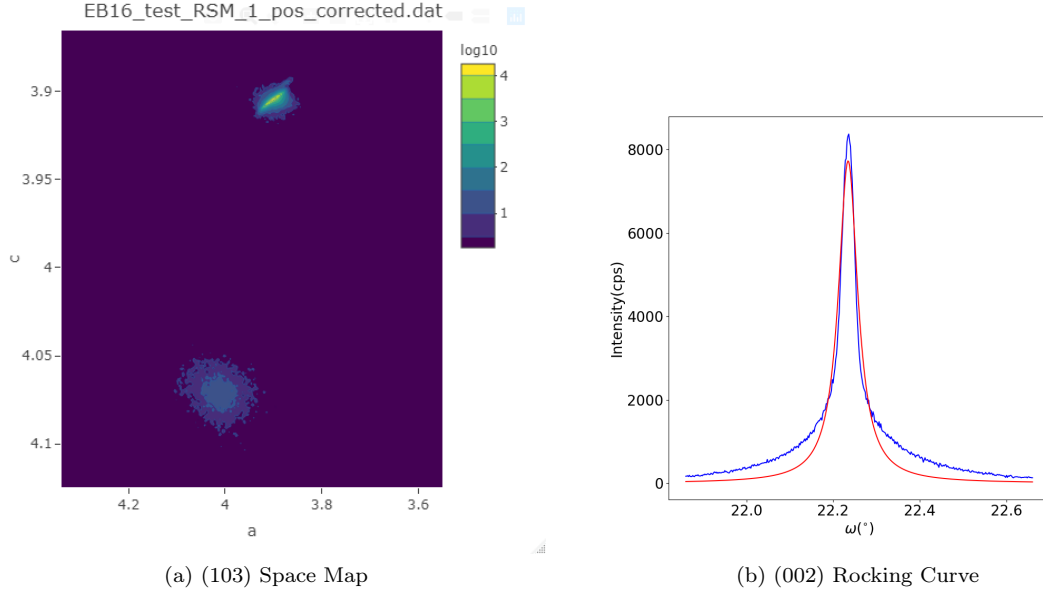

(a) (103) Space Map

(b) (002) Rocking Curve

Figure 30: Strain relaxation for deposition temperature of 550C. (a) The lattice parameters of the $SrNb_{0.05}Sn_{0.95}O_3$ are a=4.00Å and c=4.08Å. (b) The experimental data has a FWHM=0.041°.
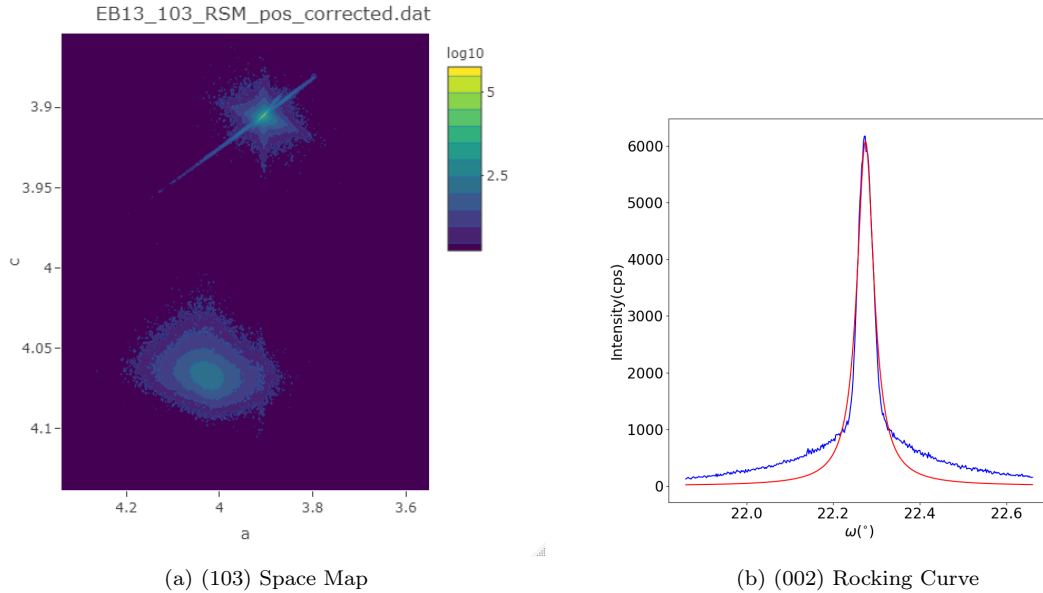

(a) (103) Space Map

(b) (002) Rocking Curve

Figure 31: Strain relaxation for deposition temperature of 600C. (a) The lattice parameters of the $SrNb_{0.05}Sn_{0.95}O_3$ are a=4.02Å and c=4.07Å. (b) The experimental data has a FWHM=0.045°.

(a) (103) Space Map

(b) (002) Rocking Curve

Figure 32: Strain relaxation for deposition temperature of 650C. (a) The right lattice parameters of the $SrNb_{0.05}Sn_{0.95}O_3$ are a=4.12Åand c=4.06Å. The left lattice parameters are a=3.92Åand c=4.08Å. (b) The experimental data has a FWHM=0.616°.
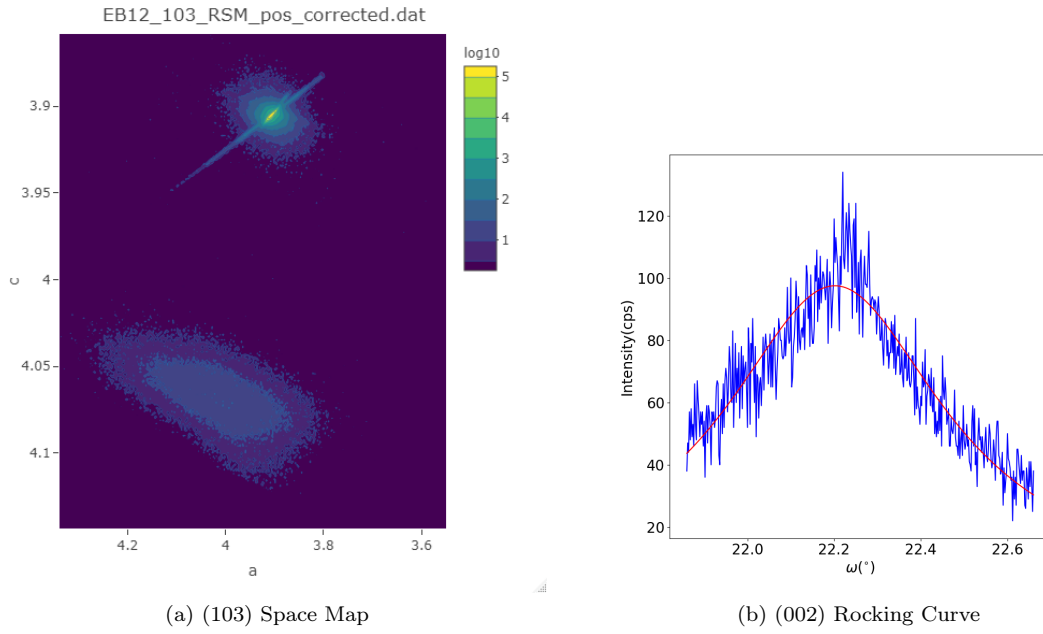

(a) (103) Space Map

(b) (002) Rocking Curve
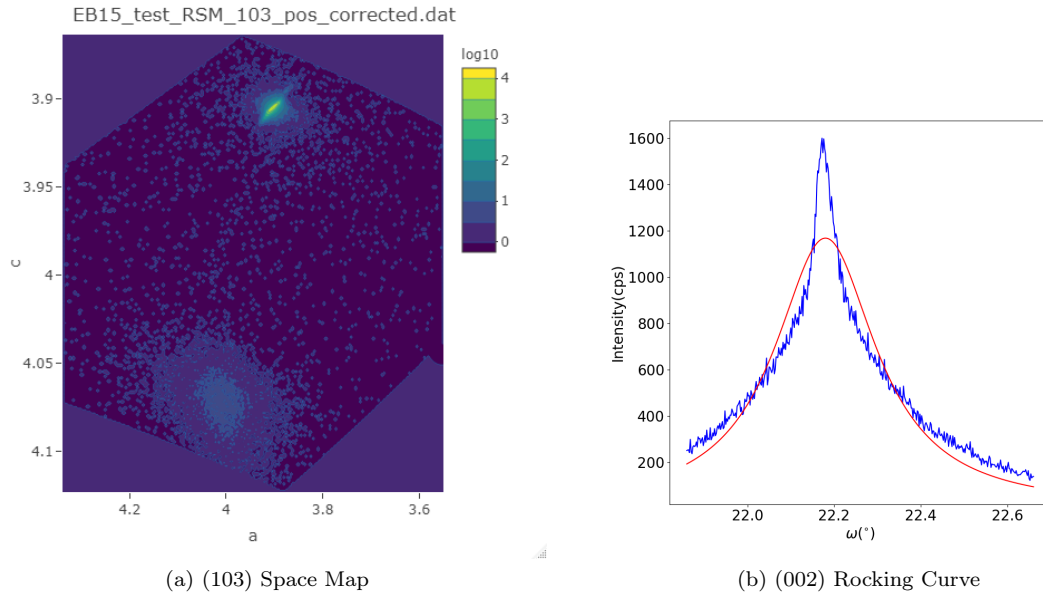
Figure 33: Strain relaxation for deposition temperature of 700C. (a) The lattice parameters of the $SrNb_{0.05}Sn_{0.95}O_3$ are a=4.01Åand c=4.07Å. (b) The experimental data has a FWHM=0.134°.

6.6 Electrical characterization $SrNb_{0.05}Sn_{0.95}O_3$

To verify the usefulness of Nb doped $SrSnO_3$ as a n-channel material, it is essential to electrically characterize the deposited thin films. An attempt is made to characterize the transport properties of the Nb doped thin film deposited at 650C. The properties to characterize are the sheet resistivity,

the charge carrier density and the charge carrier mobility. These attempts were largely unsuccessful, mainly due to the non-optimal sample geometry and the high sample resistance encountered. The transport measurements involve van der Pauw measurements and Hall measurements to determine respectively the sheet resistivity (ρ) and the charge carrier density (n_S). The van der Pauw measurements led to well defined results in a temperature range of 315K to 400K, see Fig. 34 and Fig. 35. However the Hall measurement did not yield reliable data, seef Fig. 36 . Subsequently it is not possible to determine the charge carrier mobility (μ) due to its dependence on both the sheet resistivity and the charge carrier density according to $\mu=1/\rho n_S$.
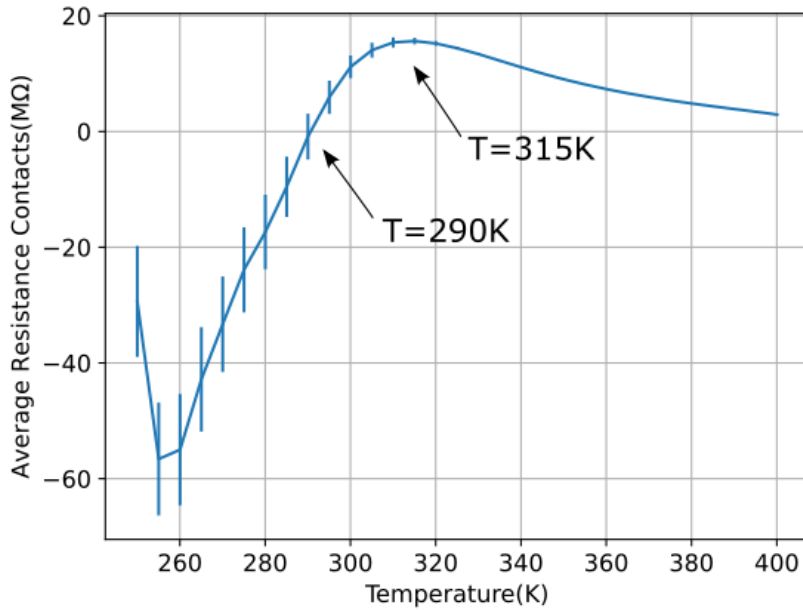
Figure 34: Average contact resistances measured over temperature for $\mathrm{Nb}_{0.05}\mathrm{Sr}_{0.95}\mathrm{SnO}_3$ on $SrTiO_3$ grown at 650C. A peak in resistance can be seen at roughly 315K. The standard deviation increases considerably for temperatures lower than 325K. Around 290K the resistance becomes negative, indicating a breakdown of the measurement apparatus.

Figure 35: Sheet resistivity vs temperature.

Figure 36: Charge carrier density vs temperature.

6.7 Conclusion

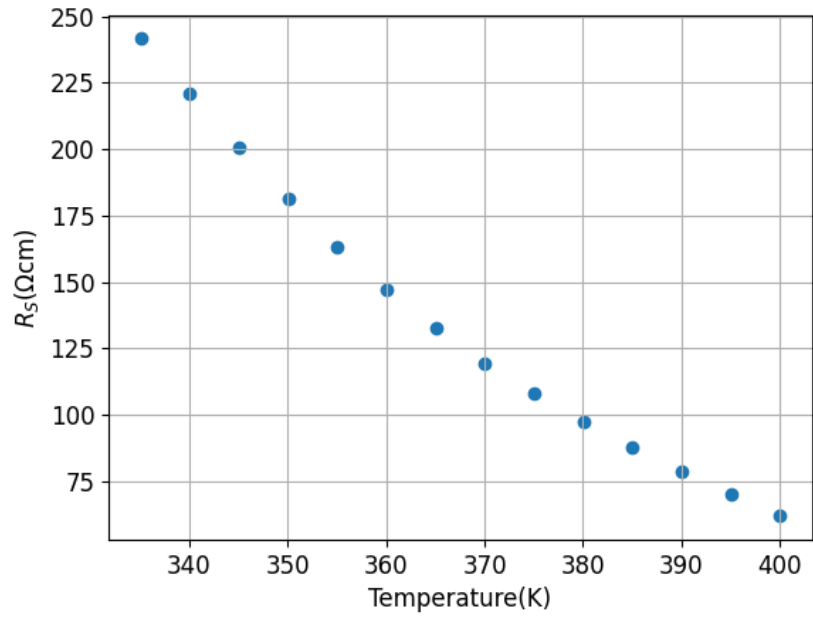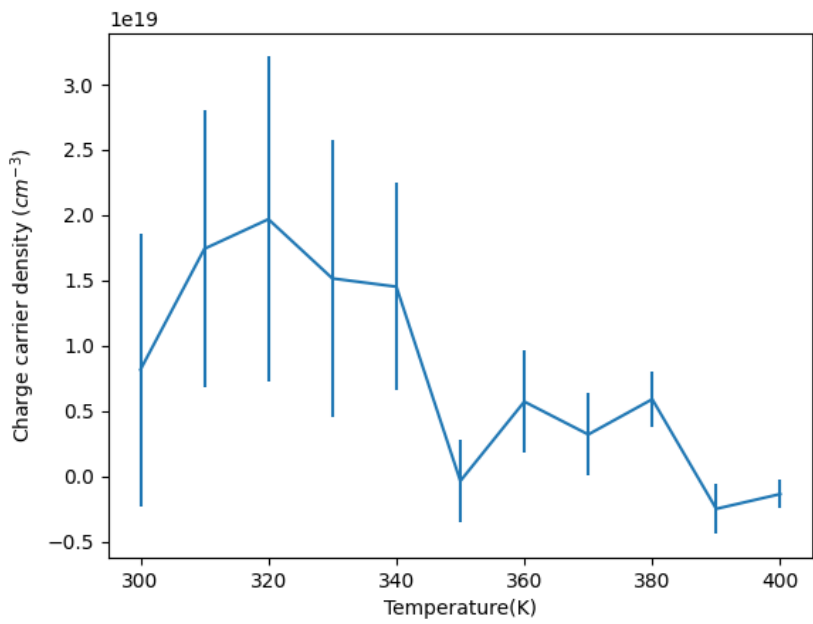The optimal deposition temperature of the $Nb_{0.05}Sr_{0.95}SnO_3$ films seems to be 600C. The results found by the surface characterization indicate that the smoothest film grows at an deposition temperature of 600C. Lower deposition temperatures lead to the formation of grains with amorphous grain boundaries, higher deposition temeperatures lead to island formation with heights of 40-50% of the deposited film. The structural characterization reveals the non-epitaxial growth of the strained $Nb_{0.05}Sr_{0.95}SnO_3$ film at 600C with an in-plane lattice parameter of 4.02Å, which is in between the a and c lattice parameter of $BaTiO_3$. The purpose of $Nb_{0.05}Sr_{0.95}SnO_3$ is to be used as an n-channel material so it may still grow epitaxially on an underlying $SrSnO_3$ film. The electrical measurements can be seen as in-conclusive, the sample geometries measured over are sub-optimal due to the high sheet resistivity of $SrSnO_3$ and the resulting experimental data is only reliable for the Van der Pauw measurements from 315K to 400K. The found sheet resistivity values are also not encouraging due to being at the order of 100 Ωcm instead of 100 mΩcm. Improving upon the electrical measurements is recommended before drawing final conclusion about the suitability of Nb doped $SrSnO_3$ as an n-channel material.

7 Electrical characterization of two terminal Ti/BaTiO$_3$/Y$_{0.05}$Sr$_{0.95}$SnO$_3$ devices

The initial scope of the project involved the search for a/c domain formation in strain engineered $BaTiO_3$ for memristive applications. However, as of yet, these domains have not been discovered. The strained $BaTiO_3$ films may still possess flexoelectric properties and will have oxygen vacancies present in the film or interface. These phenomena may still lead to memristive properties in the strained $BaTiO_3$. So two terminal devices have been manufactured with the goal of studying polarization switching and characterization of the electric properties. These two terminal devices consists of an Nb:STO substrate with Y doped $SrSnO_3$ grown on top to strain the $BaTiO_3$ film into an out-plan polarization. The electrical characterization mainly progressed to the point of defining the major conduction mechanisms at play over an voltage range of -5V to +5V. Possible switching behaviour was observed, but not characterized in detail.
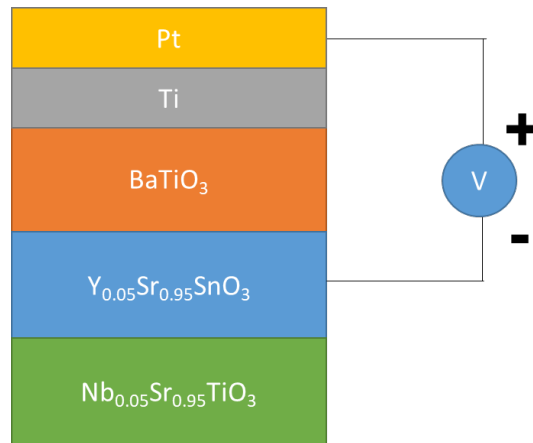

Figure 37: Two terminal device. The top electrodes consist of 10nm Ti and 90nmPt, the $BaTiO_3$ film is roughly 40nm thick and the $Y_{0.05}Sr_{0.95}SnO_3$ film is roughly 16nm thick. The $Y_{0.05}S_{0.95}SnO_3$ layer has been contacted using reactive ion beam etching, allowing the application of a voltage (V) without measuring over the $Y_{0.05}Sr_{0.95}SnO_3/Nb_{0.05}Sr_{0.95}TiO_3$ interface.

Fabrication of the two terminal devices involved the development of top electrodes on the $BaTiO_3$ film using spin-coating and UV-photolithography. The contacts are formed by sputtering 10nm of Ti and 90nm of Pt on the developed sample. The YSSO layer is contacted by using reactive ion beam etching and sputtering of Ti/Pt electrodes using a hard mask.

7.1 Current-Voltage characteristics

The current-voltage (IV) characteristics of two terminal devices have been measured for a variety of devices differing in the doping of the $SrSnO_3$ layer. An recurring issue was the high resistance encountered when measuring the IV-characteristics over the Ti electrode and the substrate, so the YSSO layer is contacted immediatley. The measured current-voltage (IV) characteristics are converted to current density-electric field measurements (JE), assuming the current density to depend on the area of the top electrode pad and the electric field by the voltage drop over the insulating $BaTiO_3$ film.
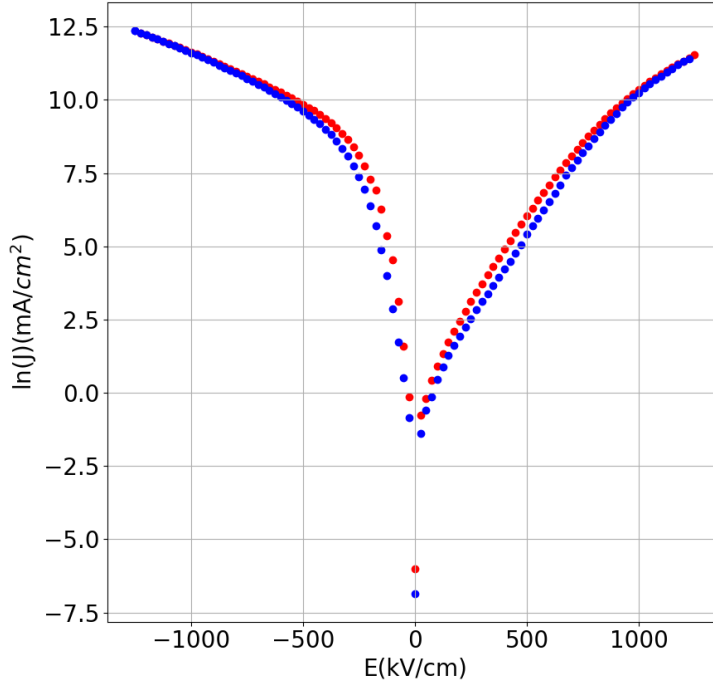
Figure 38: Current density (J) vs electric field (E). The current density is logarithmically plotted against the applied electric field. A clear asymmetry is present in the JE plot. Some hysteresis is present, the JE-sweep starts (red) at positive bias and sweeps back (blue) from negative bias.

The JE plot (Fig. 38) shows a clear asymmetry, indicating different conduction mechanisms dominating under positive and negative bias. The conduction behaviour will be analyzed separately at positive and negative bias. The hysteresis remains largely unexplained, all though it does not seem to be caused by polarization switching due to the sweep starting at positive bias and going to negative bias while the current density remains higher over the whole range, than the sweep from negative to positive bias. Polarization switching would manifest itself as an low resistance at a certain bias leading to an high resistance at opposite bias [53]. The JE data is analysed using five different conduction mechanisms; Schottky emission, Poole-Frenkel emission, Fowler-Nordheim tunneling, Variable Range Hopping and Space Charge Limited Current. Schottky emission as a conduction mechanism is relevant when the energy barrier at the interface is dominant. Fowler-Nordheim tunneling is relevant at high electric fields. The remaining three conduction mechanisms are mostly relevant in the case of bulk dominant conduction.

7.2 Interface dominant conduction

In the case of negative bias fitting for Schottky emission gives the best results. The measurement of JE-characteristics over a range of temperatures also allows the extraction of parameters associated with Schottky emission, such as the Richardson constant and the Schottky barrier height. Schottky emission is a conduction mechanism based on thermionic emission, meaning that a thermally excited charge carrier passes over the energy barrier at the cathode-semiconductor interface after which the charge carrier is transported through the conduction band into the anode by drift from the electric field[54][55]. The Schottky emission equation is:

$$J = A^* T^2 exp(-\frac{\phi_{SE} - \sqrt{e^3 E/4\pi\epsilon_0 K}}{k_B T})$$

(25)

where J is current density, A^* the Richardson constant, T the temperature, ϕ_{SE} the Schottky barrier height, E the electric field and K the optical dielectric permittivity. The first term in the exponent representing the barrier height at zero bias and the second term the modulation by the electric field. The Richardson constant relates current density to thermionic emission by $A^* = \lambda A$, with A being $4\pi m e k_B^2/h^3$. The factor λ is a material dependent correction factor. The Richardson constant varies over a range of 32 to 160 $Acm^{-2}K^{-2}$ for crystalline metals and over an greater range of values for oxides and composites[56].

To determine if Schottky emission is the dominant conduction mechanism it is usefull to define a linear relation between electric field (E) and current density (J) according to:

$$ln(J) = ln(A^* T^2) + \frac{\phi}{k_B T} - \sqrt{\frac{e^3 E}{4\pi\epsilon_0 K}}$$

(26)

$$ln(J) \propto K^{-1/2} E^{+1/2}$$

(27)

So plotting the logarithm of the current density vs the square root of the electric field should give a value for the dielectric optical constant which can be compared to literature. The optical dielectric constant is in the range of K=2.1 to K=6.2, the exact value varies considerably in literature [57][58]. The experimental values found for K lay in the range of 2.37 to 5.56, see Fig. 39 and 40. The found values for the optical dielectric constant (K) are in agreement with literature concluding that the conduction behaviour for negative bias can be indeed described by Schottky emission. The value of K does change with temperature, while the current density should increase with temperature the modulation of the Schottky barrier by the electric field should be independent of temperature. The reason of the difference in K could be due to non-linear contributions by the electric field becoming more relevant at higher temperatures [54].

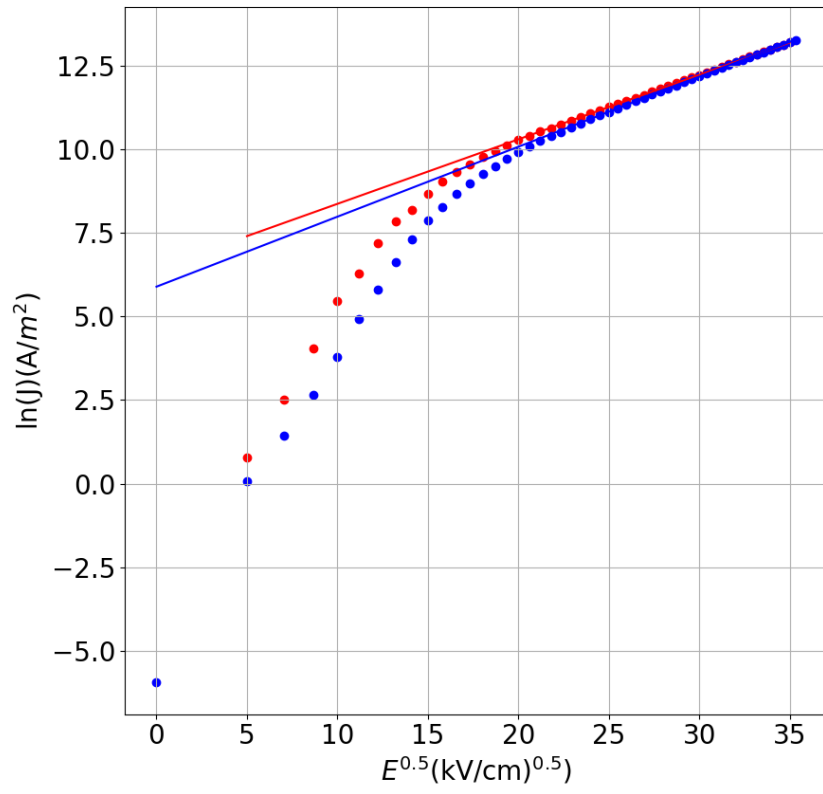Figure 39: Fit for Schottky Emission at negative bias at temperature of 30C. The straight line is fitted for both the 0V to -5V (red) and the -5V to 0V (blue) sweeps, giving respectively a K=5.56 and K=4.73. The data is fitted for -2V to -5v.
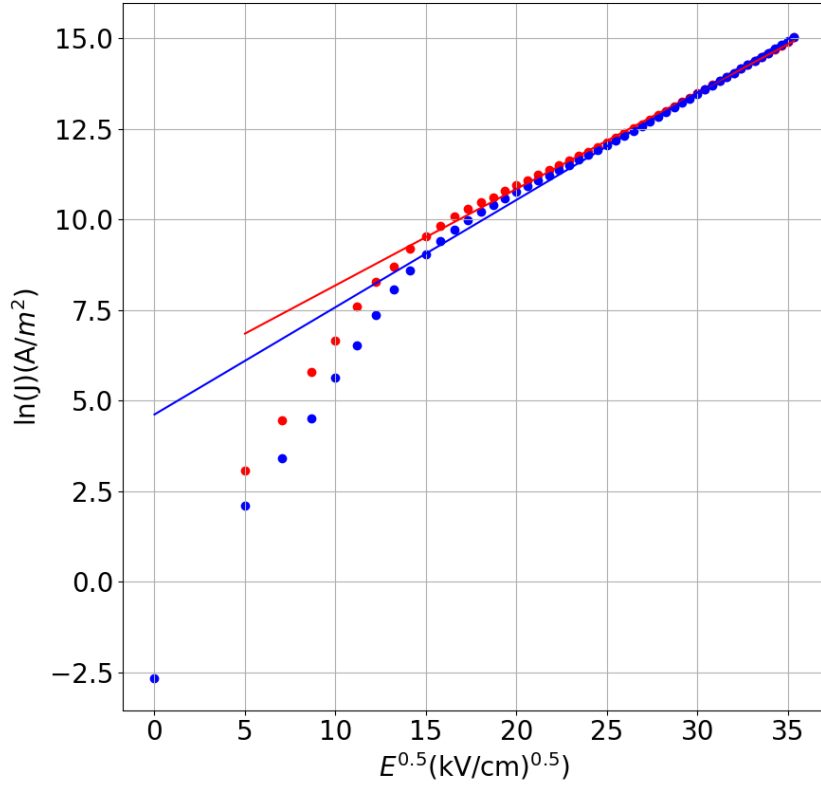
Figure 40: Fit for Schottky Emission at negative bias at temperature of 130C. The straight line is fitted for both the 0V to -5V (red) and the -5V to 0V (blue) sweeps, giving respectively a K=2.93 and K=2.37. The data is fitted for -2V to -5v.

Furthermore it is possible to study Schottky Emission in higher detail by extracting both the Richardson constant and the Schottky barrier height from temperature dependent current density vs electric field measurements. These properties can be extracted from experimental data using Richardson plots based on the following relation:

$$ln(\frac{J}{T^2}) = ln(A^*) - \frac{q}{k_B T}\phi_{app} \tag{28}$$

where J is the current density, A^* the Richardson constant and ϕ_{app} the apparent Schottky barrier height. Plotting the Richardson plots gives the apparent Schottky barriers and Richardson constants in Fig. 41 and table 4.

Figure 41: Richardson plot for voltages in range of 0.1V to 0.5V.

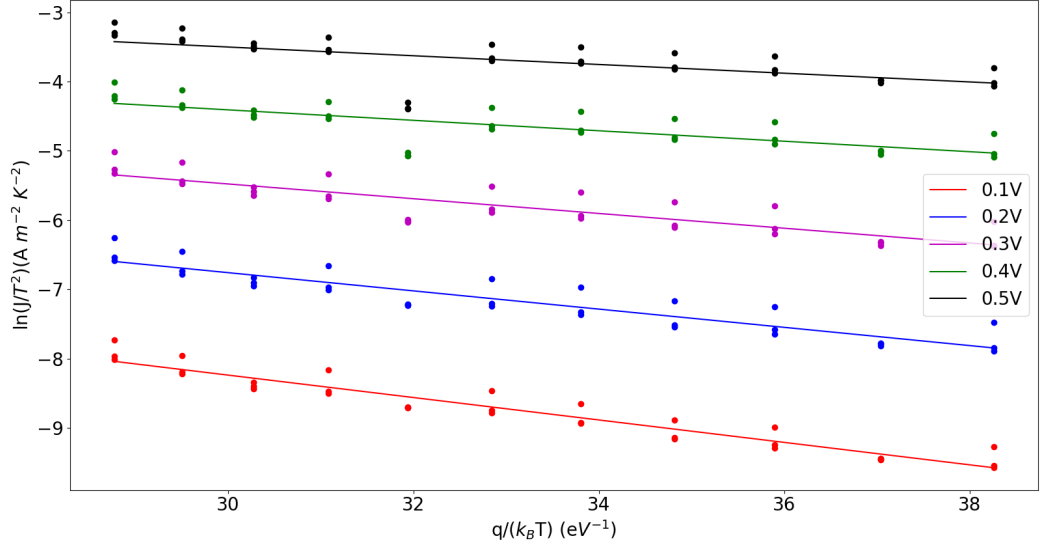| Bias Voltage(V)	Apparent Schottky Barrier (eV)	Richardson Constant ($Acm^{-2}K^{-2}$)
0.1	0.16	340
0.2	0.13	601
0.3	0.11	1018
0.4	0.08	1172
0.5	0.06	1996

Table 2: Values of apparent Schottky barrier and Richardson constant for different voltages.

From the apparent Schottky barrier height it is possible to extract the Schottky barrier height at zero electric field by noting:

$$\phi_0 = \phi_{app} - \sqrt{\frac{eE}{4\pi\epsilon_0 K}} \tag{29}$$

with ϕ_0 being the zero bias Schottky barrier and ϕ_{app} the apparent Schottky barrier height and $\sqrt{E}$ the square root of the electric field. Plotting the apparent Schottky barrier height versus the square root of the electric field allows the determination of the Schottky barrier height from the intercept. Furthermore the Richardson constant is linearly related to the electric field. The intercepts of the plots in Fig. 42 and 43 give a Schottky barrier of 0.246 $\pm$ 0.008 eV and an Richardson constant 0f $5\times10^1 \pm 9\times10^1$ $Acm^{-2}K^{-2}$. Based on the work function of Ti and the electron affinity of $BaTiO_3$, an Schottky barrier of 0.5eV would be expected at the Ti:BaTiO$_3$ interface. Furthermore an Richardson constant of several hundreds of $Acm^{-2}K^{-2}$ would also be expected for an perovskite, such as BaTiO$_3$ [59]. The deviation from the ideal Schottky barrier is expected due to the ability of interface states to significantly lower the Schottky barrier with a few tens of eV[60]. If a TiO$_x$ layer is present, this insulating layer could possibly act as the Schottky barrier [61].
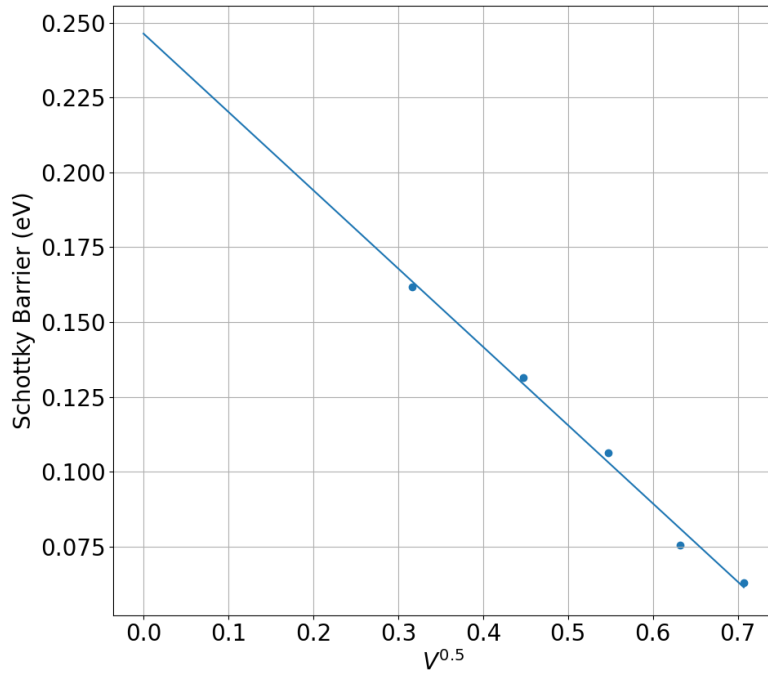
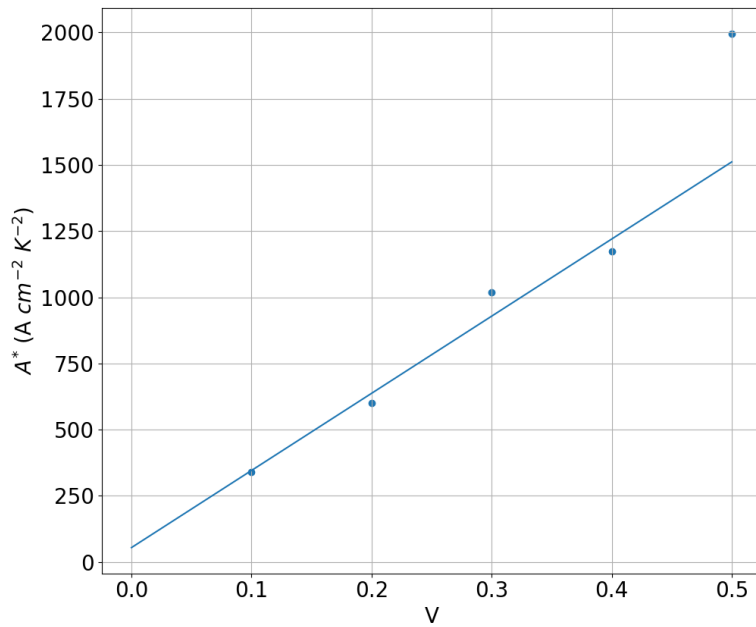Figure 42: Intercept Schottky barrier with a value of 0.25eV.

Figure 43: Intercept Richardson constant with a value of 54.2 $Acm^{-2}K^{-2}$.

7.3 Bulk dominant conduction

Under positive bias the electrical characterization involves three conduction mechanisms. These are Variable Range Hopping (VRH) mechanism, Poole-Frenkel (PF) emission and Fowler-Nordheim (FN) tunnelling. The VRH and PF conduction mechanisms are defect based and occur for up to +4V or E kV/cm. Under an high electric field FN tunnelling dominates. Furthermore also fits have been made for Space Charge Limited Current, however for positive bias the current density has an exponential dependence on the electric field.

At low electric field it is possible that the Variable Range Hopping conduction mechanism is dominant. The concept behind Variable Range Hopping states that an electron will try to find the lowest activation energy and the shortest hopping distance, leading to an optimum hopping distance with maximal hopping probability[62]. The conductance G=I/V is related to temperature as:

$$G \propto exp(-B/T^{\nu}) \tag{30}$$

where ν is an rational number related to more specific cases of Variable Range Hopping. Two cases possible cases are Mott (M-VRH) and Effros and Shklovskii (ES-VRH) variable range hopping, giving respectively $\nu=1/4$ and $\nu=1/2$.

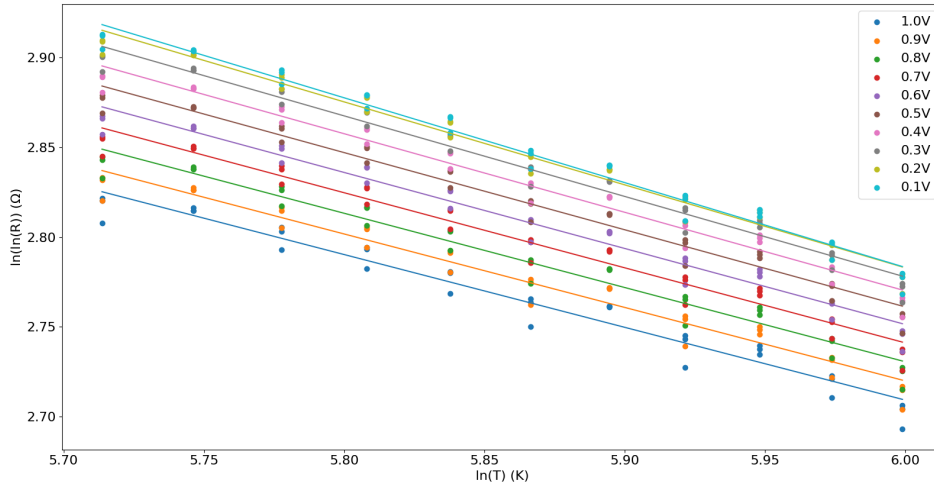Figure 44: Plot of double natural logarithm of resistance vs natural logarithm of temperature.

Bias Voltage(V)	Exponential Temperature, ν
0.1	0.472
0.2	0.462
0.3	0.449
0.4	0.438
0.5	0.430
0.6	0.423
0.7	0.418
0.8	0.414
0.9	0.409
1.0	0.405

Table 3: Values of exponent temperature dependence for different bias voltage. $\nu=0.43 \pm 0.03$.

An analysis of the temperature dependence of the resistance for positive bias in the range of 0V to 1V gives $\nu=0.43 \pm 0.03$. The found value for ν does not show a clear relation to a certain rational number, so it is not possible to connect the found experimental value to a specific case of variable range hopping. To analyze variable range hopping in more detail it may be useful to measure IV-characteristics at sub-100K temperatures [62]. The JE-characteristics in the range of 300K to 400K do not show clear variable range hopping at low electric field, but also does not exclude the variable range hopping mechanism.

The positive bias regime shows interesting behaviour in the intermediate electric field regime (+2V to +4V) in which Poole-Frenkel emission seems to dominate. This mechanism assumes the thermal ionization of trapped carriers into the conduction band, described by:

$$J = BEexp(-\frac{E_I - \sqrt{e^3 E / \pi \epsilon_0 K}}{k_B T}) \tag{31}$$

$$ln(J/E) = K^{-1/2} E^{1/2} \tag{32}$$

where B is an constant, E_I is the trap ionization energy, E the electric field, J the current density and K the optical dielectric permittivity. To determine if Poole-Frenkel emission is a suitable conduction mechanism in the intermediate regime, it is useful to linearly fit for K using equation 32. The experimental values found for the optical dielectric constant are $K=5.19$ and $K=3.84$, while literature values range from $K=2.1$ to $K=6.2$. The found experimental K values are in agreement with literature so it is reasonable to say that the intermediate electric field regime is dominated by Poole-Frenkel emission. Depending on the exact definition of the intermediate electric field regime the value of K may shift but stays within the bounds of literature values.
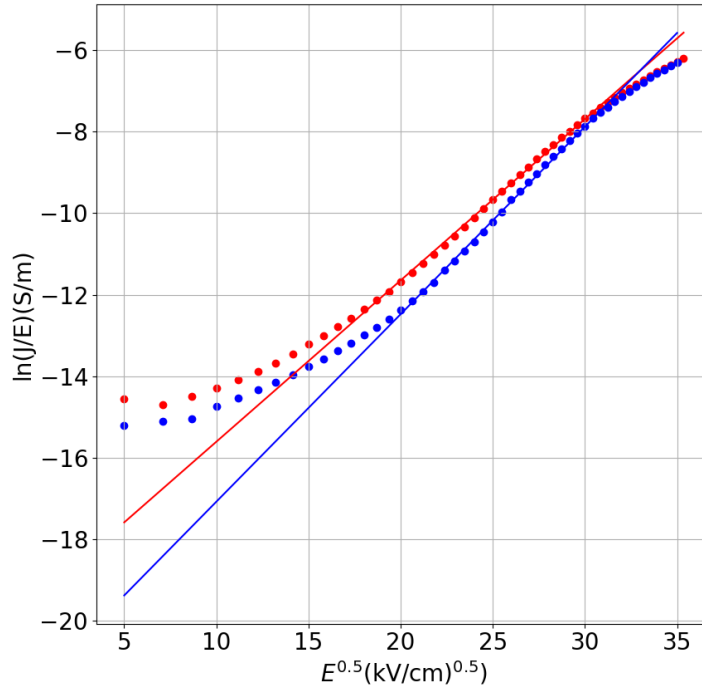

Figure 45: Poole-Frenkel Emission fitted in the intermediate regime for positive bias of +2V to +4V. The voltage sweep of +2V to +4V (red) gives $K=5.19$ and the voltage sweep of +4V to +2V (blue) gives $K=3.84$.

The high electric field regime for voltages higher than (+4V) cannot be described by Poole-Frenkel or Schottky emission, but seems to be most well described by Fowler-Nordheim (FN) tunneling. In FN tunneling a electron tunnels from the electrode into the conduction band through the bulk of an insulator, this mechanism will be most relevant at high electric fields for which the conduction band of the insulator lines up with the Fermi level of the electrode within a reasonable distance of the electrode. The Fowler-Nordheim tunneling equation is[63]:

$$J = CE^2 exp(-\frac{D^2\phi^{3/2}}{E})$$ (33)

$$C = \frac{e^3 m_0}{16\pi^2\hbar m_{eff}\phi}$$ (34)

$$D^2 = \frac{4(2m_{eff})^{1/2}}{3e\hbar}$$ (35)

where E is the electric field, ϕ is the barrier height and m_0 and m_{eff} are respectively the electron mass in free space and the effective mass. To determine if Fowler-Nordheim tunneling is relevant, the following relation can be plotted:

$$ln(\frac{J}{E^2}) \propto -D^2\phi^{3/2}E^{-1}$$ (36)

The ability to plot a straight line in the range of +4V to +5V with the values found for the two sets of data gives a plausible reason to assume Fowler-Nordheim tunneling after the intermediate electric field region in which Poole-Frenkel emission is dominant.
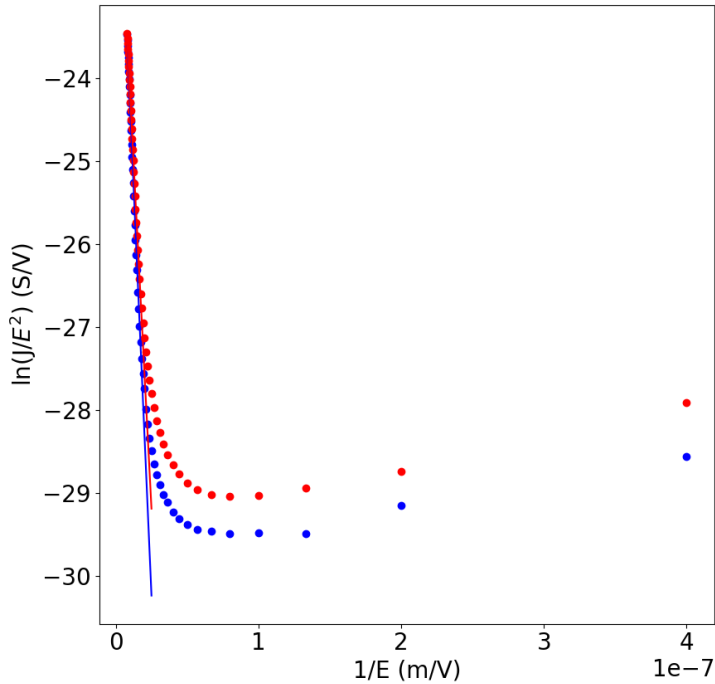

Figure 46: Fowler-Nordheim tunnelling becomes relevant possibility for higher voltages.
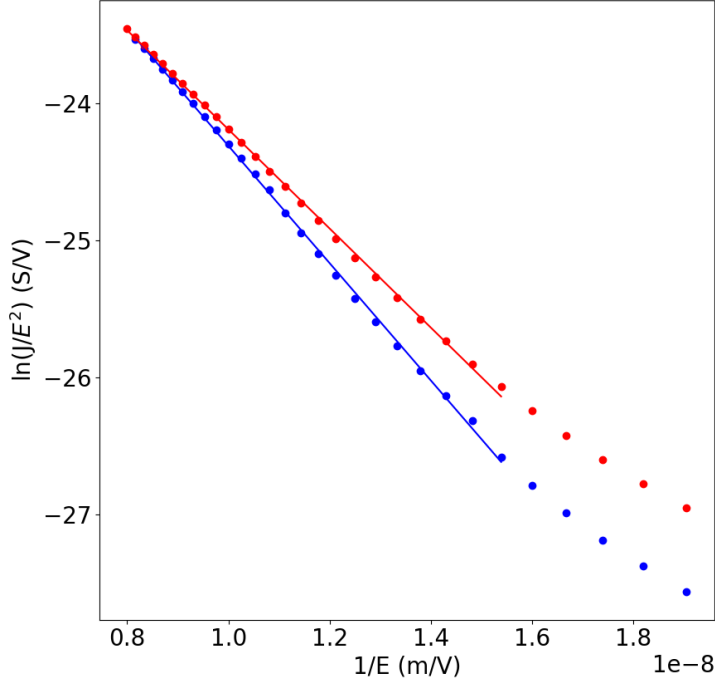
Figure 47: Fowler-Nordheim tunneling fitted in range of 0.8-1.3 m/V (+3 to +5V).

	C	$D^2\phi^{3/2}$
Blue	2.00e-09	2.07e+04
Red	1.16e-09	1.90e+04

Table 4: Parameters found for fitting the Fowler-Nordheim equation

7.4 Conclusion

Summarising the conduction behaviour of the $Ti/BaTiO_3/Y_{0.05}Sr_{0.95}SnO_3$ stack; the positive bias regime is dominated by defect based conduction until the electric field becomes strong enough to facilitate tunneling from the electrode into the conduction band. The negative bias regime is dominated by Schottky emission, indicating a upward band bending at the $Ti:BaTiO_3$ interface, assuming the electron being the charge carrier. The assymetry in the JE-characteristics can inhibit polarization switching, so it is useful to decrease the Schottky barrier. The Schottky barrier could be made smaller by using different electrode materials. However the presence of interface states makes tuning of the Schottky barrier complex to predict and leads to empirically testing of different electrode materials the only clear method of finding out the optimal electrode material. Furthermore after an better understanding of the interface between the electrode and the $BaTiO_3$, polarization switching and capacitance-voltage measurements should lead to the further determination of electrical properties. Understanding the physical mechanism and electrical properties of the $Ti/BaTiO_3/Y_{0.05}Sr_{0.95}SnO_3$ stack can also be used to determine time scales and scenarios in which memristive properties can emerge.

8   Outlook

The master research project has lead to some advancement in the direction of fabricating a low strain $BaTiO_3$ FeFET, however much work still needs to be done. The experimental work needs to be expanded upon to reach stronger conclusion. The expanding on the experimental work should not only consist of varying additional parameters in sample fabrication, but also consist of using new experimental techniques. Additional spectroscopy techniques could provide additional information over the properties of the doped $SrSnO_3$ and strained $BaTiO_3$. For example, the effects of dopants on $SrSnO_3$ could be studied with x-ray photon spectroscopy, while Raman spectroscopy could provide additional information over flexoelectricity in $BaTiO_3$. The novel ferroelectric phases which are the goal of the project due to their possible memristive properties are not found. The strain engineering necessary to produce the novel ferroelectric phases is not precise enough. To summarise, the growing, fabricating and measuring of samples needs to be performed with an higher degree of precision to reach better results.

References

[1] F. Akopyan, J. Sawada, A. Cassidy, R. Alvarez-Icaza, J. Arthur, P. Merolla, N. Imam, Y. Naka-mura, P. Datta, G.-J. Nam, B. Taba, M. Beakes, B. Brezzo, J. B. Kuang, R. Manohar, W. P. Risk, B. Jackson, and D. S. Modha, "Truenorth: Design and tool flow of a 65 mw 1 million neuron programmable neurosynaptic chip," *IEEE Transactions on Computer-Aided Design of Integrated Circuits and Systems*, vol. 34, no. 10, pp. 1537–1557, 2015.

[2] R. Groningen, "Overview of expertise in cognigron," 2020.

[3] J. del Valle, J. G. Ramírez, M. J. Rozenberg, and I. K. Schuller, "Challenges in materials and devices for resistive-switching-based neuromorphic computing," *Journal of Applied Physics*, vol. 124, no. 21, p. 211101, 2018.

[4] N. K. Upadhyay, H. Jiang, Z. Wang, S. Asapu, Q. Xia, and J. Joshua Yang, "Emerging memory devices for neuromorphic computing," *Advanced Materials Technologies*, vol. 4, no. 4, p. 1800589, 2019.

[5] J. von Neumann, *The Computer and the Brain*. Yale University Press, 2012.

[6] C. Zamarreño-Ramos, L. Camuñas-Mesa, J. Pérez-Carrasco, T. Masquelier, T. Serrano-Gotarredona, and L.-B. B., "On spike-timing-dependent-plasticity, memristive devices, and building a self-learning visual cortex," *Front. Neurosci*, vol. 5.

[7] L. Chua, "Memristor-the missing circuit element," *IEEE Transactions on Circuit Theory*, vol. 18, no. 5, pp. 507–519, 1971.

[8] H. T. Tour, James M., "The fourth element," *Nature*, vol. 453, pp. 42–43, 2008.

[9] A. G. Alharbi and M. H. Chowdhury, *Memristor Emulator Circuits*. Springer Nature Switzerland AG 2021: Springer, Cham, 2021.

[10] L. Chua and S. M. Kang, "Memristive devices and systems," *Proceedings of the IEEE*, vol. 64, no. 2, pp. 209–223, 1976.

[11] D. B. Strukov, G. S. Snider, D. R. Stewart, and R. S. Williams, "The missing memristor found," *Nature*, vol. 453, no. 7191, pp. 80–83, 2008.

[12] A. Chanthbouala, V. Garcia, R. O. Cherifi, K. Bouzehouane, S. Fusil, X. Moya, S. Xavier, H. Yamada, C. Deranlot, N. D. Mathur, M. Bibes, A. Barthélémy, and J. Grollier, "A ferro-electric memristor," *Nature Materials*, vol. 11, no. 10, pp. 860–864, 2012.

[13] A. Everhardt, "Novel phases in ferroelectric batio3 thin films: Enhanced piezoelectricity and low hysteresis.," *Rijksuniversiteit Groningen*, 2017.

[14] A. H. G. Vlooswijk, "Structure and domain formation in ferroelectric thin films," *Rijksuniversiteit Groningen*, 2009.

[15] R. E. Cohen, "Origin of ferroelectricity in perovskite oxides," *Nature*, vol. 358, no. 6328, pp. 136–138, 1992.

[16] H. Liu and X. Yang, "A brief review on perovskite multiferroics," *Ferroelectrics*, vol. 507, no. 1, pp. 69–85, 2017.

[17] A. V. Hippel, "Ferroelectricity, domain structure, and phase transitions of barium titanate," *Rev. Mod. Phys.*, vol. 22, no. 3, pp. 221–237, 1950.

[18] R. R. Mehta, B. D. Silverman, and J. T. Jacobs, "Depolarization fields in thin ferroelectric films," *Journal of Applied Physics*, vol. 44, no. 8, pp. 3379–3385, 1973.

[19] C. Kittel, "Physical theory of ferromagnetic domains," *Rev. Mod. Phys.*, vol. 21, pp. 541–583, Oct 1949.

[20] V. G. Koukhar, N. A. Pertsev, and R. Waser, "Thermodynamic theory of epitaxial ferroelectric thin films with dense domain structures," *Physical Review B*, vol. 64, 2001.

[21] A. Grünebohm, M. Marathe, and C. Ederer, "Ab initio phase diagram of batio3 under epitaxial strain revisited," *Applied Physics Letters*, vol. 107, no. 10, p. 102901, 2015.

[22] E. V. Bursian, O. I. Zaikovskii, and K. V. Makarov, "Ferroelectric plate polarization by bending," *Izv. Akad. Nauk, SSSR Ser. Fiz. 33 1098–102*, 1969.

[23] P. Zubko, G. Catalan, A. Buckley, P. R. L. Welche, and J. F. Scott, "Strain-gradient-induced polarization in srtio3 single crystals," *Phys. Rev. Lett.*, 2007.

[24] P. V. Yudin and A. K. Tagantsev, "Fundamentals of flexoelectricity in solids," *Nanotechnology*, vol. 24, no. 43, p. 432001, 2013.

[25] P. Zubko, G. Catalan, and A. K. Tagantsev, "Flexoelectric effect in solids," *Annual Review of Materials Research*, vol. 43, no. 1, pp. 387–421, 2013.

[26] D. Lee, A. Yoon, S. Y. Jang, J.-G. Yoon, J.-S. Chung, M. Kim, J. F. Scott, and T. W. Noh, "Giant flexoelectric effect in ferroelectric epitaxial thin films," *Phys. Rev. Lett.*, vol. 107, p. 057602, 2011.

[27] G. Catalan, A. Lubk, A. H. G. Vlooswijk, E. Snoeck, C. Magen, A. Janssens, G. Rispens, G. Rijnders, D. H. A. Blank, and B. Noheda, "Flexoelectric rotation of polarization in ferroelectric thin films," *Nature Materials*, vol. 10, pp. 963–967, 2011.

[28] J. Očenášek, H. Lu, C. W. Bark, C. B. Eom, J. Alcalá, G. Catalan, and A. Gruverman, "Nanomechanics of flexoelectric switching," *Phys. Rev. B*, vol. 92, p. 035417, 2015.

[29] P. Selvarajan, G. Chandra, S. Bhattacharya, S. Sil, A. Vinu, and S. Umapathy, "Potential of raman spectroscopy towards understanding structures of carbon-based materials and perovskites," *Emergent Materials*, vol. 2, pp. 417–439, 2019.

[30] A. Aziz, E. T. Breyer, A. Chen, X. Chen, S. Datta, S. K. Gupta, M. Hoffmann, X. S. Hu, A. Ionescu, M. Jerry, T. Mikolajick, H. Mulaosmanovic, K. Ni, M. Niemier, I. O'Connor, A. Saha, S. Slesazeck, S. K. Thirumala, and X. Yin, "Computing with ferroelectric fets: Devices, models, systems, and applications," pp. 1289–1298, 2018.

[31] X. Chen, X. Yin, M. Niemier, and X. S. Hu, "Design and optimization of fefet-based crossbars for binary convolution neural networks," pp. 1205–1210, 2018.

[32] H. Mulaosmanovic, J. Ocker, S. Müller, M. Noack, J. Müller, P. Polakowski, T. Mikolajick, and S. Slesazeck, "Novel ferroelectric fet based synapse for neuromorphic systems," pp. T176–T177, 2017.

[33] I. Vrejoiu, G. LeRhun, L. Pintilie, D. Hesse, M. Alexe, and U. Gösele, "Intrinsic ferroelectric properties of strained tetragonal pbzr$_{0.2}$ti$_{0.8}$o$_3$ obtained on layer–by–layer grown, defect–free single–crystalline films," *Advanced Materials*, vol. 18, no. 13, pp. 1657–1661, 2006.

[34] F. Aubriet, N. Chaoui, R. Chety, B. Maunit, E. Millon, and J.-F. Muller, "Laser ablation mass spectrometry: a tool to investigate matter transfer processes during pulsed-laser deposition experiments," *Applied Surface Science*, vol. 186, no. 1, pp. 282–287, 2002.

[35] H. M. Christen and G. Eres, "Recent advances in pulsed-laser deposition of complex oxides," *Journal of Physics: Condensed Matter*, vol. 20, no. 26, p. 264005, 2008.

[36] R. Eason, "Pulsed laser deposition of thin films: Applications-led growth of functional materials," 2006.

[37] A. S. Paulo and R. García, "Tip-surface forces, amplitude, and energy dissipation in amplitude-modulation (tapping mode) force microscopy," *Phys. Rev. B*, vol. 64, p. 193411, Oct 2001.

[38] N. Jalili and K. Laxminarayana, "A review of atomic force microscopy imaging systems: application to molecular metrology and biological sciences," *Mechatronics*, vol. 14, no. 8, pp. 907–945, 2004.

[39] S. Magonov, "Chapter 10 - visualization of polymers at surfaces and interfaces with atomic force microscopy," in *Handbook of Surfaces and Interfaces of Materials* (H. S. Nalwa, ed.), pp. 393–430, Burlington: Academic Press, 2001.

[40] S. Csiszár and L. Tjeng, *X-ray diffraction and X-ray absorption of strained CoO and MnO thin films.* PhD thesis, 2005.

[41] H. Akima, "A new method of interpolation and smooth curve fitting based on local procedures," *J. ACM*, vol. 17, no. 4, p. 589–602, 1970.

[42] M. Lee, "X-ray diffraction for materials research: From fundamentals to applications," *MRS Bulletin*, vol. 42, 2017.

[43] G. Cao, *Nanostructures & Nanomaterials: Synthesis, Properties & Applications.* EngineeringPro collection, Imperial College Press, 2004.

[44] J. Horkstra, L. J. Van der Pauw, and N. Philips, "Measurement of the resistivity constants of anistotropic conductors by means of plane-parallel discs of arbitrary shape†," *Journal of Electronics and Control*, vol. 7, no. 2, pp. 169–171, 1959.

[45] L. van der Pauw, "A method of measuring specific resistivity and hall effects of discs of arbitrary shape.," *Philips Research Reports*, vol. 13, pp. 1–9, 1958.

[46] T. Truttmann, A. Prakash, J. Yue, T. E. Mates, and B. Jalan, "Dopant solubility and charge compensation in la-doped $srsno_3$ films," *Applied Physics Letters*, vol. 115, no. 15, p. 152103, 2019.

[47] E. Baba, D. Kan, Y. Yamada, M. Haruta, H. Kurata, Y. Kanemitsu, and Y. Shimakawa, "Optical and transport properties of transparent conducting la-doped $srsno_3$ thin films," *Journal of Physics D: Applied Physics*, 2015.

[48] Y. Kumar, R. Kumar, R. Choudhary, A. Thakur, and A. Singh, "Reduction in the tilting of oxygen octahedron and its effect on bandgap with la doping in $srsno_3$," *Ceramics International*, vol. 46, no. 11, Part A, pp. 17569–17576, 2020.

[49] S. M. de Freitas, G. J. Júnior, R. D. Santos, and M. V. dos S. Rezende, "Defects and dopant properties of srsno3 compound: A computational study," *Computational Condensed Matter*, vol. 21, p. e00411, 2019.

[50] K. Li, Q. Gao, L. Zhao, and Q. Liu, "Electrical and optical properties of nb-doped srsno3 epitaxial films deposited by pulsed laser deposition," *Nanoscale Research Letters*, vol. 15, p. 164, 2020.

[51] B. Li, Q. Liu, Y. Zhang, Z. Liu, and L. Geng, "Highly conductive nb doped $basno_3$ thin films on mgo substrates by pulsed laser deposition," *Journal of Alloys and Compounds*, vol. 680, pp. 343–349, 2016.

[52] Q. Liu, J. Dai, X. Zhang, G. Zhu, Z. Liu, and G. Ding, "Perovskite-type transparent and conductive oxide films: Sb- and nd-doped $srsno_3$," *Thin Solid Films*, vol. 519, no. 18, pp. 6059–6063, 2011.

[53] H. Matsuo, Y. Kitanaka, R. Inoue, Y. Noguchi, and M. Miyayama, "Switchable diode-effect mechanism in ferroelectric bifeo$_3$ thin film capacitors," *Journal of Applied Physics*, vol. 118, no. 11, p. 114101, 2015.

[54] C. Kenney, K. C. Saraswat, B. Taylor, and P. Majhi, "Thermionic field emission explanation for nonlinear richardson plots," *IEEE Transactions on Electron Devices*, vol. 58, no. 8, pp. 2423–2429, 2011.

[55] M. Gülnahar and H. Efeoğlu, "Double barrier nature of au/p-gate schottky contact: Linearization of richardson plot," *Solid-State Electronics*, vol. 53, no. 9, pp. 972–978, 2009.

[56] B. Wolf, *Handbook of ion sources*. CRC Press, 1995.

[57] S. Wemple, M. Didomenico, and I. Camlibel, "Dielectric and optical properties of melt-grown batio3," *Journal of Physics and Chemistry of Solids*, vol. 29, no. 10, pp. 1797–1803, 1968.

[58] R. Thomas, D. Dube, M. Kamalasanan, and S. Chandra, "Optical and electrical properties of batio3 thin films prepared by chemical solution deposition," *Thin Solid Films*, vol. 346, no. 1, pp. 212–225, 1999.

[59] W. Zhang, J. Ouyang, H. Cheng, Q. Yang, L. Kang, H. Zhang, and F. Hu, "Interface charge behaviors of BaTiO3 film heterostructures with various crystal orientations," *Japanese Journal of Applied Physics*, vol. 56, no. 2, p. 020304, 2017.

[60] W. Mönch, "Metal-semiconductor contacts: electronic properties," *Surface Science*, vol. 299-300, pp. 928–944, 1994.

[61] H. Fan, C. Chen, Z. Fan, L. Zhang, Z. Tan, P. Li, Z. Huang, J. Yao, G. Tian, Q. Luo, Z. Li, X. Song, D. Chen, M. Zeng, J. Gao, X. Lu, Y. Zhao, X. Gao, and J.-M. Liu, "Resistive switching and photovoltaic effects in ferroelectric batio3-based capacitors with ti and pt top electrodes," *Applied Physics Letters*, vol. 111, no. 25, p. 252901, 2017.

[62] D. Yu, C. Wang, B. L. Wehrenberg, and P. Guyot-Sionnest, "Variable range hopping conduction in semiconductor nanocrystal solids," *Phys. Rev. Lett.*, vol. 92, p. 216802, 2004.

[63] N. M. Ravindra and J. Zhao, "Fowler-nordheim tunneling in thin SiO2films," *Smart Materials and Structures*, vol. 1, no. 3, pp. 197–201, 1992.